Long-term in vivo calcium imaging of astrocytes reveals distinct cellular compartment responses to sensory stimulation

Stobart, Jillian L ; Ferrari, Kim David ; Barrett, Matthew J P ; Stobart, Michael J ; Looser, Zoe J ; Saab, Aiman S ; Weber, Bruno

Abstract: Localized, heterogeneous calcium transients occur throughout astrocytes, but the characteristics and long-term stability of these signals, particularly in response to sensory stimulation, remain unknown. Here, we used a genetically encoded calcium indicator and an activity-based image analysis scheme to monitor astrocyte calcium activity in vivo. We found that different subcellular compartments (processes, somata, and endfeet) displayed distinct signaling characteristics. Closer examination of individual signals showed that sensory stimulation elevated the number of specific types of calcium peaks within astrocyte processes and somata, in a cortical layer-dependent manner, and that the signals became more synchronous upon sensory stimulation. Although mice genetically lacking astrocytic IP3R-dependent calcium signaling (Ip3r2−/−) had fewer signal peaks, the response to sensory stimulation was sustained, suggesting other calcium pathways are also involved. Long-term imaging of astrocyte populations revealed that all compartments reliably responded to stimulation over several months, but that the location of the response within processes may vary. These previously unknown characteristics of subcellular astrocyte calcium signals provide new insights into how astrocytes may encode local neuronal circuit activity.

DOI: https://doi.org/10.1093/cercor/bhw366

Long-term *in vivo* calcium imaging of astrocytes reveals distinct cellular compartment responses to sensory stimulation

Jillian L. Stobart*[1,2], Kim David Ferrari*[1,2], Matthew J.P. Barrett[1,2], Michael J. Stobart[1,2], Zoe J. Looser[1,2], Aiman S. Saab[1,2], Bruno Weber[1,2]

(1) Institute of Pharmacology and Toxicology, University of Zurich, Winterthurerstrasse 190, CH-8057 Zurich, Switzerland
(2) Neuroscience Center, University and ETH Zurich, Winterthurerstrasse 190, CH-8057 Zurich, Switzerland

* These authors contributed equally to this work.

Abstract

Localized, heterogeneous calcium transients occur throughout astrocytes, but the characteristics and long-term stability of these signals, particularly in response to sensory stimulation, remain unknown. Here, we used a genetically-encoded calcium indicator and an activity-based image analysis scheme to monitor astrocyte calcium activity *in vivo*. We found that different sub-cellular compartments (processes, somata and endfeet) displayed distinct signaling characteristics. Closer examination of individual signals showed that sensory stimulation elevated the number of specific types of calcium peaks within astrocyte processes and somata, in a cortical layer-dependent manner, and that the signals became more synchronous upon sensory stimulation. Although mice genetically lacking astrocytic IP3R-dependent calcium signaling (*Ip3r2*$^{-/-}$) had fewer signal peaks, the response to sensory stimulation was sustained, suggesting other calcium pathways are also involved. Long-term imaging of astrocyte populations revealed that all compartments reliably responded to stimulation over several months, but that the location of the response within processes may vary. These previously unknown characteristics of sub-cellular astrocyte calcium signals provide new insights into how astrocytes may encode local neuronal circuit activity.

Keywords

calcium transients, GCaMP6s, somatosensory cortex, two photon microscopy, whisker barrels

Astrocytes, the primary glial cell type in the cortex, may influence synaptic environments, neuronal metabolism, and local blood flow. However, debate exists over the astrocytic contribution to these mechanisms, particularly *in vivo* (Takata et al. 2011; Navarrete et al. 2012; Nizar et al. 2013; Bonder and McCarthy 2014; Otsu et al. 2015). Central to this debate is the physiological role of astrocyte intracellular calcium fluctuations that are considered a measure of astrocyte activity and are potentially linked to the modulation of neuronal function (Volterra et al. 2014).

Classical studies of astrocyte calcium signaling *in vivo* have used calcium indicator dyes, which primarily detect calcium surges within astrocyte somata (Wang et al. 2006; Takata and Hirase 2008; Nizar et al. 2013) but not fine processes (Shigetomi et al. 2013). Recently, *in vivo* calcium imaging has been greatly improved by the development of genetically encoded calcium indicators (GECIs), such as the GCaMP family, which can be specifically expressed in astrocytes and label the entire cellular structure (Shigetomi et al. 2013; Gee et al. 2014; Kanemaru et al. 2014). This labelling of cortical, olfactory bulb and hippocampal astrocytes has revealed spontaneous calcium signals that are diverse in their cellular localization (endfoot, soma, and process) and signal characteristics (Bonder and McCarthy 2014; Gee et al. 2014; Kanemaru et al. 2014; Asada et al. 2015; Otsu et al. 2015; Srinivasan et al. 2015; Tang et al. 2015). However, the relevance of this signal heterogeneity to astrocyte brain function remains unclear (Volterra et al. 2014).

Cortical astrocyte calcium signaling also occurs in response to sensory stimulation (Wang et al. 2006; Takata et al. 2011; Gee et al. 2014), and may encode neuronal responses to different patterns of sensory input (Volterra et al. 2014). Fine astrocyte processes are closely associated with synapses, and could respond to synaptic activity with discrete calcium signals that are confined to the local structure. Also, astrocyte calcium signals can be synchronized between different cellular compartments and neighbouring cells (Takata and Hirase 2008). This synchronicity could be essential for astrocyte integration of activity from a cortical network. Additionally, astrocytes have been shown to have

different levels of spontaneous activity between cortical layers (Takata and Hirase 2008), suggesting astrocyte populations may also have unique layer cyto-architectures similar to cortical neuronal networks (Petersen 2007).

Here, we investigated how astrocyte calcium signal heterogeneity may encode synaptic activity by examining astrocyte calcium signals evoked by sensory input in order to determine if sub-cellular regions (endfeet, somata, and processes) have similar responses, temporal synchronicity and long-term stability. We imaged GCaMP6s in somatosensory astrocytes *in vivo* and developed novel analysis tools that enabled us to discriminate between spontaneous and sensory-evoked activity within the astrocyte population, characterize distinct peak types, and monitor astrocyte calcium signals over several months. Our results indicate that active regions within somatosensory astrocytes respond to sensory input with calcium signals of a particular shape, that these regions become more synchronized upon stimulation, and that the response varies between cortical layers. Furthermore, the overall response in all sub-cellular compartments was stable over several months. This work provides new insight into how calcium signaling in different astrocytic compartments may reflect local synaptic activation evoked by sensory stimulation.

Materials and Methods

Cloning and virus production

The GCaMP6s gene from pGP-CMV-GCaMP6s (a gift from Douglas Kim; Addgene plasmid #40753 (Chen et al. 2013)) was cloned into a plasmid backbone containing AAV2 inverted terminal repeats, a short GFAP promoter (Gfa-ABC$_1$D or sGFAP (Lee et al. 2008)), a β-globin intron, and poly adenylation signal (Mächler et al. 2016). This plasmid was packaged into adeno-associated virus (AAV) serotype 9 (AAV9-sGFAP-GCaMP6s) by the University of North Carolina Vector Core.

Animals

All experimental procedures were approved by the local veterinary authorities, conforming to the guidelines of the Swiss Animal Protection Law, Veterinary Office, Canton Zurich (Act of Animal Protection 16 December 2005 and Animal Protection Ordinance 23 April 2008). Mice were housed under an inverted 12-hour light/dark cycle. *Ip3r2* mice were maintained as a heterozygous line and genotypes were determined using previously reported mutant allele-specific primers (Li et al. 2005). Female C57BL/6J (Charles River) or *Ip3r2*$^{-/-}$ mice with wild-type littermates (*Ip3r2*$^{+/+}$; Li et al. 2005; Di Castro et al. 2011) were surgically prepared at eight to ten weeks of age.

Head post implantation

Surgery was conducted as previously described (Mayrhofer et al. 2015). Under isoflurane (4% for induction, 1-2% for maintenance), animals were fixed in a stereotaxic frame and an incision was made along the midline to expose the skull. After cleaning the bone, a bonding agent (Prime & Bond) and several layers of light-cured dental cement (Tetric EvoFlow) were applied to the skull and polymerized with blue light. An aluminum head post was attached to the cement at the back of the head. The skull over the left somatosensory cortex was left exposed for later craniotomy and virus injection.

Intrinsic optical imaging

Intrinsic optical imaging (IOI) was used to map the somatosensory areas for proper localization of the virus injection and subsequent two-photon imaging. Two days following the head post surgery, the skull over the left cortex was moistened with a water based gel to increase bone transparency, and covered with a glass coverslip. Under 630 nm illumination, images were acquired using a 12-bit CCD camera (Pixelfly VGA, PCO Imaging) focused 0.4 mm below the cortical surface. Whisker (10 Hz) or hindpaw stimulation (400 µA, 1 ms, 4 Hz, 5 s) elicited increased blood flow to the corresponding sensory

area, which was observed as increased light absorption. IOI measurements were repeated 2 weeks after surgery through the cranial window to create a somatotopic map that was used for appropriate localization during two-photon imaging.

Virus injection and chronic window implantation

Under midazolam (5mg/kg), fentanyl (0.05mg/kg) and medetomidine (0.5 mg/kg) anesthesia, a craniotomy was cut over the primary sensory cortex using the IOI map as a reference. A pipette and hydraulic pump were used to inject AAV9-GFAP-GCaMP6s virus (300 nl of 3.2 x 10^{12} particles/ml at 50 nl/min) into the hindpaw and/or whisker barrel areas at a depth of 350 – 400 µm. A square cover slip (3x3 mm) was lightly pressed on the exposed brain and fixed with dental cement to the head cap.

Two-photon imaging

Imaging commenced three weeks after virus injection using a custom-built two-photon laser-scanning microscope. A 20x water immersion microscope objective was used (W Plan-Apochromat 20x/1.0 DIC VIS-IR, Zeiss). GCaMP6s was excited at 940 nm with a Ti:sapphire laser (Chameleon Ultra II; Coherent or InSight DeepSee; Spectra-Physics) with power between 10-30 mW. Fluorescence emission was detected with a GaAsP photomultiplier module (Hamamatsu Photonics) with a band pass filter BrightLine HC 520/50 and a short pass filter BrightLine 750/sp (Semrock). The two-photon laser-scanning microscope was controlled by a customised version of *ScanImage* (r3.8.1; Janelia Research Campus).

All imaging was conducted under isoflurane anesthesia (1-1.5%). Detailed anatomical images (512 x 512 pixels) of each field of view were collected at 0.74 frames per second. Images (256×256 or 128×128 pixels) were acquired at a frequency of 1.48-2.96 frames per second. Multiple fields of view in both cortical layer 1 (depth ~30-100 µm) and cortical layer 2/3 (depth ~150-250µm) were recorded in each animal. Single whiskers were threaded into a glass capillary attached to a custom-built piezoelectric

stimulator (T223-H4CL-303X; Piezo Systems) and deflected at different frequencies of stimulation (10 Hz, 20 Hz, 40 Hz, and 90 Hz; 1 or 8 s duration) during imaging. The contralateral hindpaw was electrically stimulated by a 4 Hz (1 ms pulse), 400 μA current for 5 s. Given that all mice had a chronic cranial window implanted, we were able to conduct multiple imaging sessions for each animal.

Image analysis and statistics

Image analysis was performed using ImageJ (Schneider et al. 2012) and MATLAB R2014b (MathWorks). For each field of view, all images were aligned using a 2D convolution engine to account for x-y drift in time. Background noise was defined as the bottom fifth percentile pixel value in each frame and was subtracted from every pixel. Regions of interest (ROIs) were selected by 2 methods: our customized implementation of an activity based algorithm (Ellefsen et al. 2014) and manual selection in ImageJ of somata and endfeet ROIs using high resolution (512x512 pixel) anatomical images. In the activity based algorithm, a 2D spatial Gaussian filter with $\sigma xy = 3$ pixels (2.86 μm) and a temporal moving average filter with a width of 3 frames were applied to all images to reduce noise. A moving threshold for each pixel was defined in the filtered stack as the mean intensity plus seven times the standard deviation of the same pixel during the preceding 30 frames. Using this sliding box-car approach, active pixels were identified as those that exceeded the threshold. Active pixels were grouped within a radius of 5 pixels (4.75 μm) in space and 2 frames in time. The 3D mask of active pixels was summed along the temporal dimension, normalized, and thresholded at $\theta = 0.3$ to make a 2D activity ROI mask. Raw image data from pixels within each 2D ROI were statistically compared to pixels surrounding the ROI (p-value < 0.05 by one-way ANOVA) to exclude false positives. Activity ROI masks and manually selected ROI masks (somata and endfeet) were compared and overlapping regions were excluded from the activity mask to ensure each ROI was unique. When comparing different stimulation conditions in each field of view, ROI masks were combined to measure the same ROIs in all conditions. A signal vector (dF/F) was calculated

relative to the baseline fluorescence in the first 5 seconds of the trial. This vector was low-pass filtered using a moving average filter with a cut-off frequency of ~0.03 Hz to locate plateau peaks and measure their features, such as maximum amplitude and duration (findpeaks function; MATLAB). Single peak and multi peak signals were identified by applying a digital band-pass filter with passband frequencies f1 = 0.0286 Hz and f2 = 0.1 Hz to the dF/F signal vector before running MATLAB findpeaks function. We also used a seed-based correlation analysis to correlate the signal vector (dF/F) for each ROI with the vectors from all other ROIs in the same field of view and examined the mean Pearson's correlation coefficient across trials. For chronic recordings, animals were imaged over two months at four different time points. The distance between ROI centroids from different imaging days was calculated and ROIs were considered to be the same where this distance was less than the radius of the mean ROI area.

All statistics were performed in R (version 3.1.2) using the lme4 package (Bates et al. 2015) for linear mixed-effects models. As fixed effects, we used stimulus condition (with/without stimulation), ROI type (endfoot, soma, or process), and cortical layer and also tested the interaction of these effects. As random effects, we had intercepts for individual animals, fields of view, and ROIs. Likelihood ratio tests comparing models with fixed effects against models without fixed effects were used to determine the model with the best fit while accounting for the different degrees of freedom. Visual inspection of residual plots did not reveal any obvious deviations from homoscedasticity or normality. All data were reported and plotted as uncorrected means and standard error of the means. P-values for different parameter comparisons were obtained using the lsmeans or multcomp (Hothorn et al. 2008) packages with Tukey *post-hoc* tests.

Immunohistochemistry

Mice were anesthetized with pentobarbital (>50 mg/kg) and transcardially perfused with 2% PFA. Brains were post-fixed in 4% PFA for 3 hours and cryoprotected with 30 % sucrose in PBS for 24

hours. Free-floating sections (40 µm) were cut with a freezing microtome. Slices were incubated with rabbit anti-glial fibrillary acidic protein (GFAP) antibody (*Z0334*; DakoCytomation, DK), rabbit anti-Iba1 (WAKO) or anti-rat CD68 (MCA1957GA, Serotec) together with chicken anti-GFP antibody (GFP-1020, Aves Labs). Secondary antibodies for red and green (goat anti-rabbit Alexa Fluor® 660 and goat anti-chicken Alexa Fluor® 488; Life Technologies) were then added. Images of the sections were collected with a Zeiss LSM710 confocal microscope.

Results

Astrocyte sub-cellular regions are spontaneously active and exhibit distinct signaling characteristics

To visualize astrocyte cytosolic calcium signals in the mouse somatosensory cortex, we injected AAV9-sGFAP-GCaMP6s virus, implanted a chronic cranial window, and imaged the animals by two-photon microscopy three weeks later while under isoflurane anesthesia (Fig. 1A). To analyze the GCaMP6s calcium signals recorded during two-photon imaging, we developed a semi-automated image analysis where active regions of interest (ROIs) were identified in time and space (Ellefsen et al. 2014) and condensed into a 2D mask (Fig. 1B). Somata and endfeet regions were selected by hand from visible structures in baseline images. The majority of ROIs identified by the automated analysis were located in the fine cellular processes, but those that overlapped with manually-selected somata and endfeet ROIs were excluded to ensure each ROI was distinct. Process ROIs had a greater number of spontaneous signals per minute (0.65 ± 0.02 signals/min; $P< 0.0001$; Fig. 1D) and a larger mean amplitude (0.35 ± 0.01 fold; $P< 0.0001$; Fig.1E) than endfeet or somata ROIs. However, the mean duration of spontaneous signals from somata ROIs (9.58 ± 0.32 s) was greater than processes ($P= 0.0175$) and endfeet ($P= 0.0255$; Fig. 1F). A previous study comparing Oregon Green BAPTA-AM labelled rat astrocytes in different cortical layers showed layer 1 somata were more spontaneously active with larger signal amplitudes than layer 2/3 cells (Takata and Hirase 2008). Overall, we did not observe significant differences in

spontaneous signal amplitude, duration or number of signals per minute between layers; however, layer 1 somata tended to have more signals per minute than layer 2/3 somata (Supplementary Figs. 1A-C). Notably, there was also no difference in the number of ROIs per area (mm^2) between different layers (Supplementary Fig. 1D).

Based on their shape, GCaMP6s signal peaks were also divided into three different classes: single peaks, multi peaks, and plateaus (Fig. 1G; Bonder & McCarthy 2014). These peak types were classified based on band-pass (single and multi peaks) and low-pass filtering (plateaus) of the signal fluorescence vector. Single peaks were identified as short, individual peaks, while multi peaks were oscillating signals with multiple maxima close together in time. Plateau signals were identified as long, slower signals that had a small slope (<0.0015 DF/s) at the peak maximum (Fig. 1G). Of all spontaneous peaks, 21% were single peaks, 47.2% were multi peaks and 31.8% were plateaus (n= 4839 signals; 12 mice). Multi peaks were the most frequent peak type when considering the overall number of peaks per minute per ROI ($P< 0.0001$; Fig. 1H). Multi peaks also had the largest mean amplitude (0.71 ± 0.02 fold; $P= 0.0335$ vs single peaks), while plateaus had a smaller mean amplitude (0.24 ± 0.01 fold) compared to both multi peaks ($P< 0.0001$) and single peaks (0.62 ± 0.03 fold; $P< 0.0001$; Fig. 1I). Plateau peaks had the longest mean duration (27.83 ± 0.42 s; $P< 0.0001$), while multi peaks (18.12 ± 0.11 s) were longer than single peaks (15.1 ± 0.12 s; $P< 0.0001$; Fig. 1J). The distribution of peak types within individual ROI groups was also different with endfeet and somata favouring plateaus (endfeet: 47.7% of 587 signals; somata: 53.6% of 1556 signals; 12 mice) and processes favouring multi peaks (59.3% of 2696 signals; 12 mice; Fig. 1K). Process ROI peaks had different shapes compared to endfeet and somata peaks, with larger mean amplitudes (Supplementary Fig. 1E) and significantly greater duration for multi peaks and plateaus (Supplementary Fig. 1F).

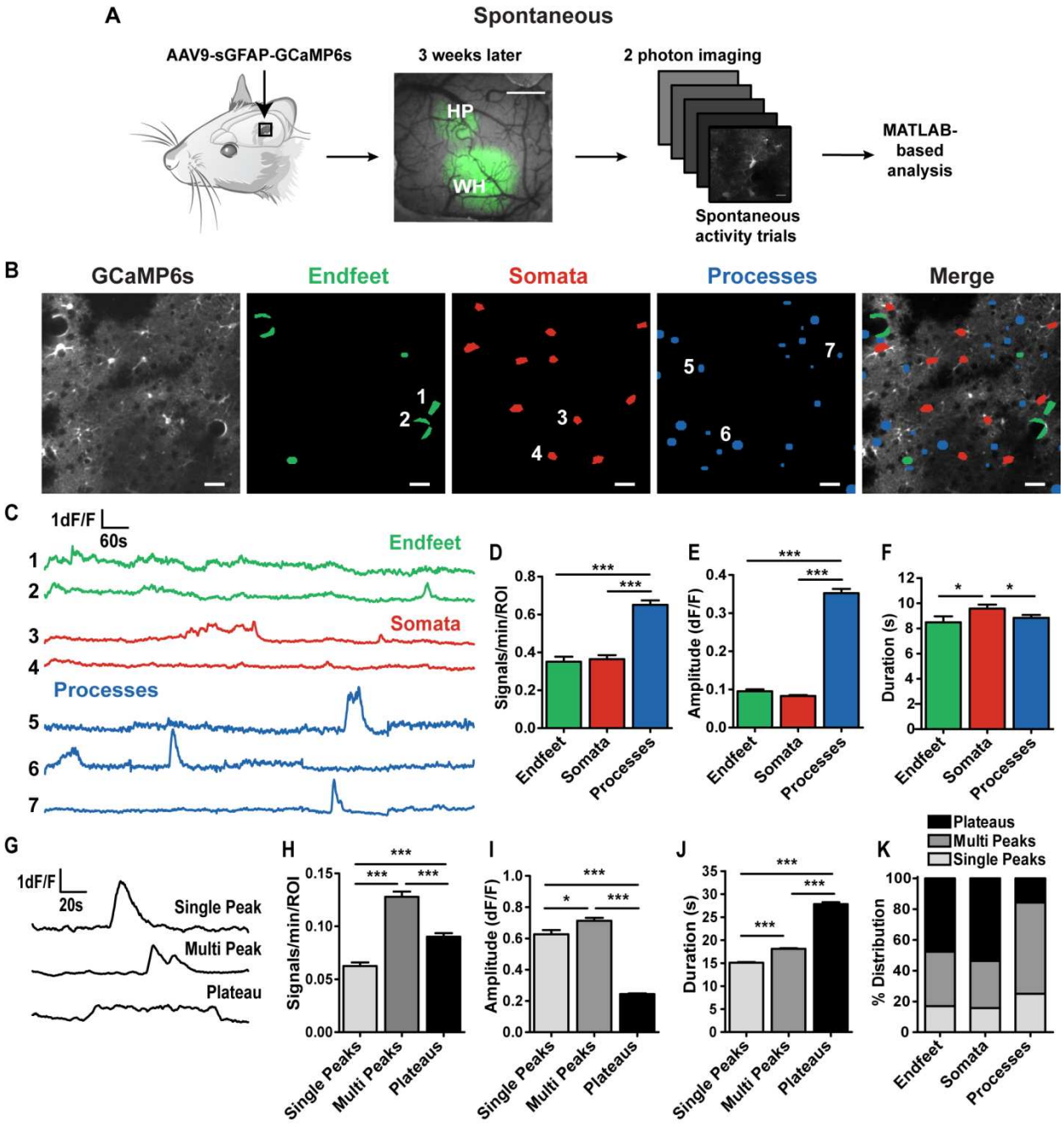

Figure 1: Astrocyte sub-cellular calcium domains exhibit distinct spontaneous signalling characteristics. (A) Left: AAV9-sGFAP-GCaMP6s virus was injected into the mouse somatosensory cortex. Middle: Example image of the chronic cranial window showing GCaMP6s expression in the whisker (WH) and hindpaw (HP) areas 3 weeks post-injection. Scale bar is 500 µm. Right: Images from anesthetized animals without stimulation were collected by two-photon microscopy and analyzed in MATLAB. (B) Endfoot (green) and soma (red) regions of interest (ROIs) were selected manually based on

visible structures. Active calcium ROIs were identified algorithmically and primarily localized in astrocyte processes (blue). Scale bar is 30 µm. (C) Example traces of spontaneous activity from each ROI type. (D-F) Mean number of signals per minute, amplitude, and duration of signals per ROI (Endfeet: n= 167 ROIs; Somata: n= 393 ROIs; Processes: n= 501 ROIs; 12 mice). (G) Example traces of the three peak types: single peaks, multi peaks and plateaus. (H) Mean number of each peak type per minute per ROI (n= 1061 ROIs; 12 mice). (I,J) Mean amplitude and duration of the different peak types (single peaks: n= 1018 signals; multi peaks: n= 2283 signals; plateaus: n= 1538 signals; 12 mice). (K) Relative percentages of each peak type within the different ROI types. Example traces were smoothed with a 5 point moving average. Bar graphs are uncorrected mean ± SEM. * $P< 0.05$, *** $P< 0.001$. Statistics calculated using linear mixed models. See also Supplementary Fig. 1.

These calcium signals were recorded from healthy astrocytes, since GCaMP6s expression co-localized with astrocyte dye, SR101, 90 min after intravenous dye injection (Fig. 2A; Appaix et al. 2012). Also, cortical virus injections did not induce reactive astrogliosis or microglial activation, as glial fibrillary acidic protein (GFAP) and ionized calcium binding adapter molecule 1 (Iba1) labelling was similar within the injection site and in the contralateral (non-injected) hemisphere (Figs. 2B-E). Additionally, we did not detect an increase in CD68 staining, further supporting a lack of microglial activation (Supplementary Fig. 2).

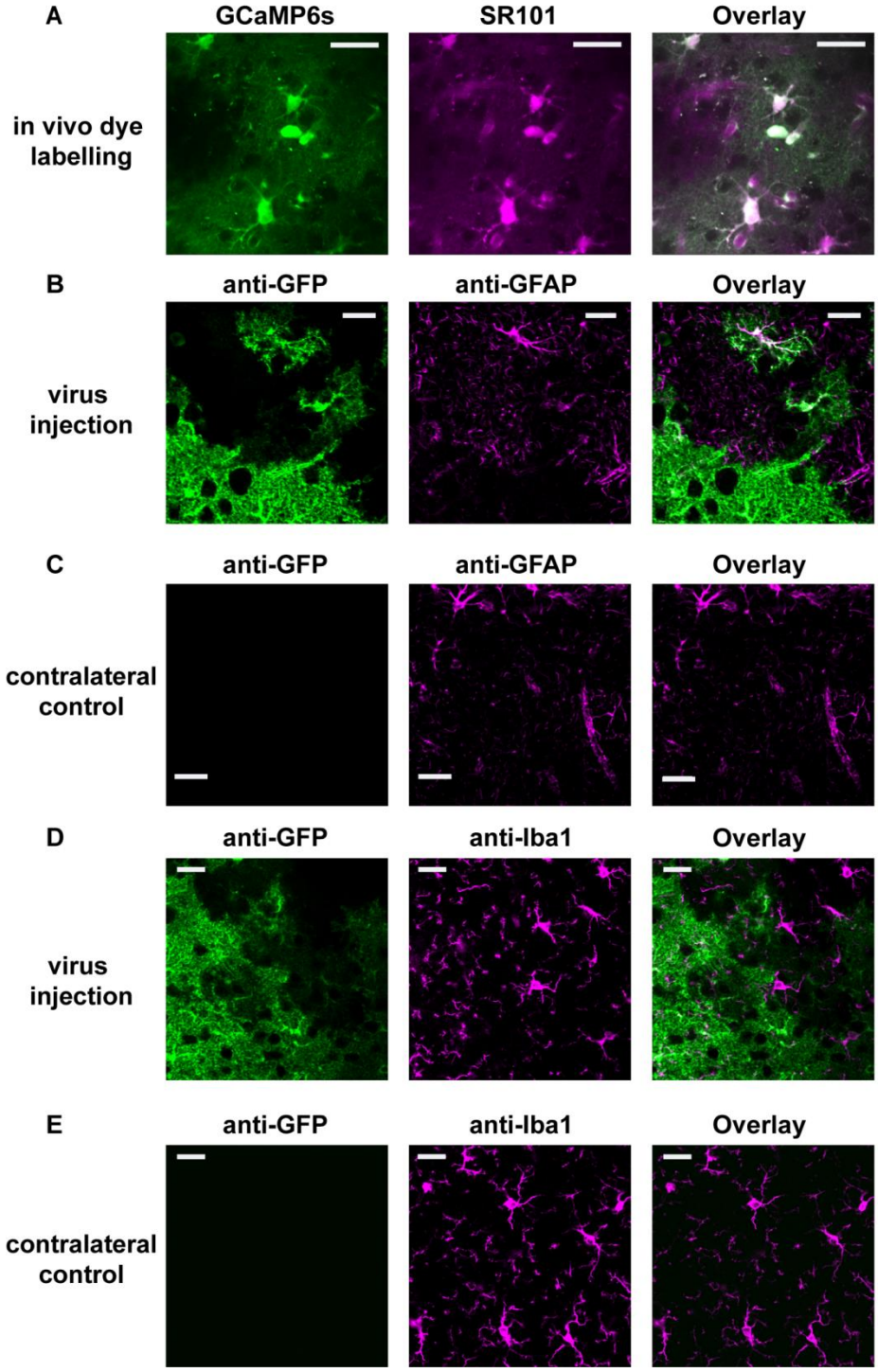

Figure 2: Astrocytic GCaMP6s expression *in vivo*. (A) Images of GCaMP6s expression and sulforhodamine 101 (SR101), a dye known to label astrocytes, taken 90 min after intravenous SR101 injection. Scale bar is 30 µm. (B) Immunohistochemistry of brain slices from AAV9-GFAP-GCaMP6s injected mice. The virus injection site (GCaMP6s) was further stained with an anti-GFP antibody and

astrocytes were labelled with anti-glial fibrillary acidic protein (GFAP). Scale bars are 20 µm. (C) Virus injected hemispheres were compared to GFAP staining on the contra-lateral (non-injected control) side. (D) Immunohistochemistry for microglial infiltration. The virus injection site was further stained with an anti-GFP antibody and microglia were labelled with anti-Iba1. (E) Virus injected hemispheres were compared to the contra-lateral side. Scale bars are 20 µm. See also Supplementary Fig. 2.

Astrocytes respond to sensory stimulation

In order to study the local astrocyte response to somatosensory activation, we used two different stimulation paradigms: electrical hindpaw stimulation (400 µA at 4 Hz for 5 s, Movie 1) and single whisker deflection (1 s duration) at different frequencies known to mimic "stick-slip" events from whisking on textured surfaces (Movie 2; (Wolfe et al. 2008; Jadhav et al. 2009; Mayrhofer et al. 2015)). We directly compared trials with sensory stimulation to trials without stimulation to identify stimulus-evoked responses. This was done by running the semi-automated ROI selection on each group of trials independently and then combining the ROIs to make an overall ROI mask that included endfeet, somata, and process ROIs. In Figure 3B, process ROI masks were generated for the same field of view from trials with one of five frequencies of whisker stimulation: 0 Hz (no stimulation), 10 Hz, 20 Hz, 40 Hz, and 90 Hz. The final combined mask (sum of all process masks, plus the manually-selected endfeet and somata mask) was then applied to all images to collect signal information from the same ROI population for each stimulus condition. When considering the entire ROI population (endfeet, somata and processes together), 90 Hz whisker stimulation ($P = 0.0025$) and hindpaw stimulation ($P < 0.0001$) increased the mean number of signals per minute per ROI compared to trials without stimulation (Fig. 3C). Lower frequencies of whisker stimulation (10-40 Hz) did not increase the number of peaks per ROI. We attributed the absence of whisker-stimulation-evoked responses at these frequencies to the high degree of spontaneous activity within many ROIs. Therefore, we defined a ROI as "responding" if it contained peaks in the 30 seconds following the onset of sensory stimulation in any trial ("activity window"); ROIs

that did not meet this criterion were defined as “spontaneous”. In the hindpaw area, ~80% of the 297 ROIs (5 mice, including endfeet, somata, and processes) showed a response in the activity window following electrical stimulation, while ~44% of 492 barrel cortex ROIs (5 mice) responded to single whisker deflection of any frequency (10 Hz - 90 Hz). The time to peak maximum after the onset of stimulation was similar at 12.95 ± 0.28 s for hindpaw stimulation (n= 804 peaks from 5 mice) and 13.89 ± 0.32 s for whisker deflection (n= 769 peaks from 5 mice; P= 0.668). When averaging the data from all trials, responding ROIs had more signals per minute (Fig. 3D) and greater mean signal amplitudes (Fig. 3E) and duration (Fig. 3F) during both types of stimulation (hindpaw and various whisker deflection frequencies) compared to no stimulation trials. In a recent study, we characterized the neuronal population response to different frequencies (0 Hz, 10 Hz, 40 Hz, 90 Hz, 110 Hz) of whisker stimulation through neuronal calcium imaging (Mayrhofer et al. 2015). We observed that the calcium signal amplitude and response probability increased sublinearly with increasing stimulation frequency; however, different stimulation frequencies elicited similar cortical network activation in the same neuronal populations (Mayrhofer et al. 2015). In the present study, astrocytes did not demonstrate a sublinear, graded response to increasing whisker stimulus frequency, but 90 Hz stimulation elicited the largest mean amplitude, duration and number of signals per minute (Figs. 3D-F) in responding ROIs. We also calculated the response probability for each astrocyte ROI (i.e. the fraction of trials with a signal in the activity window) and found that the mean probability was less than 1.0. This suggests astrocytes did not respond to the stimulus in every trial, but they responded on average in ~30% of whisker trials and ~55% of hindpaw trials (Fig. 3G). Sensory stimulation did not elicit a global astrocytic response, as no change in number of signals per minute, amplitude, or duration were detected in responding whisker barrel ROIs during hindpaw stimulation and responding hindpaw ROIs during whisker stimulation (Supplementary Fig. 3). Since whisker deflection is non-noxious and more physiological than hindpaw

stimulation and 90 Hz stimulation evokes a strong neuronal response (Mayrhofer et al. 2015), we used 90 Hz whisker stimulation for 8 seconds to evoke the maximal response in the remaining experiments.

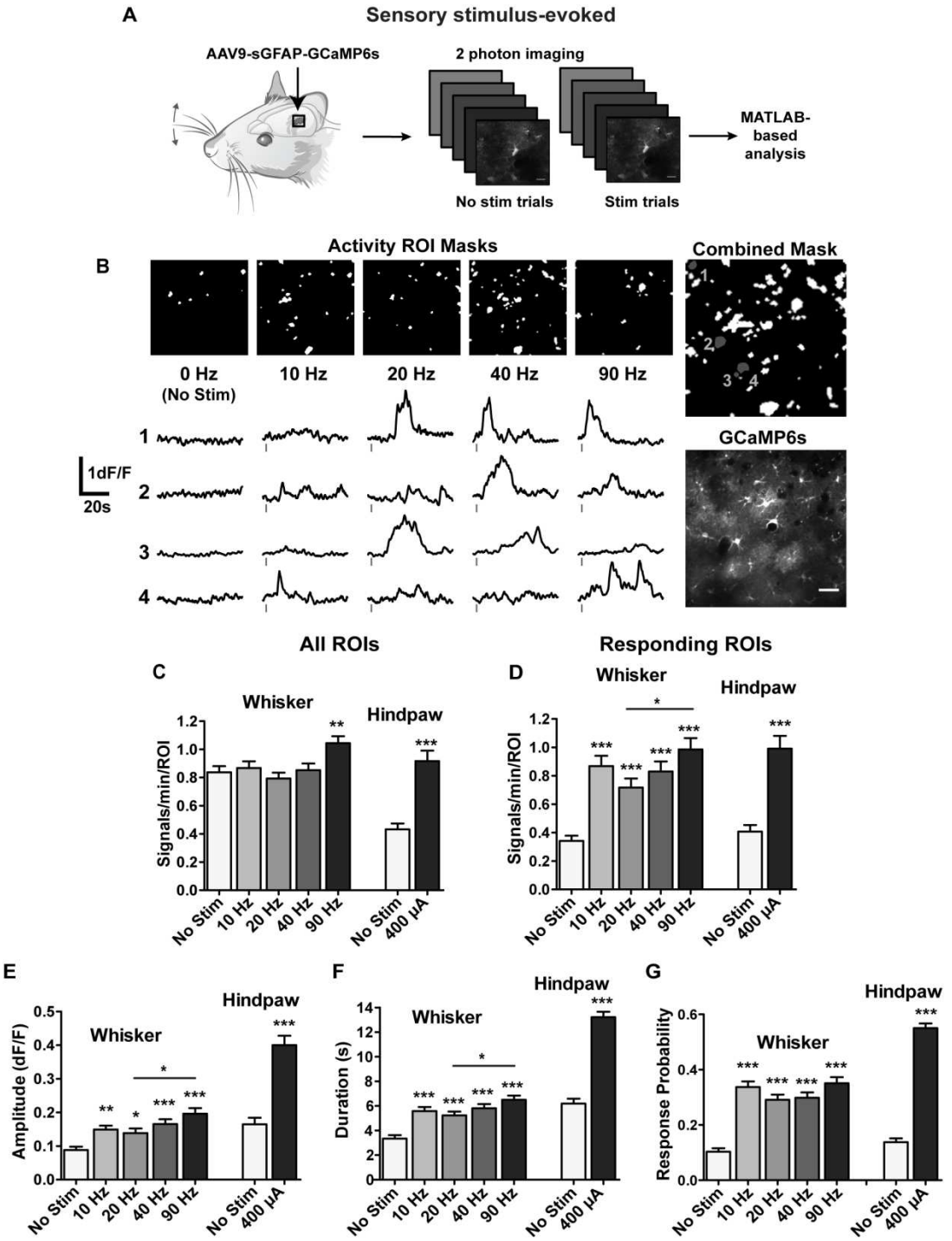

Figure 3: Astrocytes respond to sensory stimulation. (A) GCaMP6s positive astrocytes in the hindpaw and whisker cortical areas were imaged by two-photon microscopy. Images from trials with and without sensory stimulation were compared. (B) Activity ROI masks from trials without stimulation (0 Hz) and with brief (1 s) single whisker deflection (10 Hz, 20 Hz, 40 Hz, 90 Hz; top) were pooled together (combined mask; right). Scale bar is 30 μm. Lower: Example traces (smoothed with a 5 point moving average) from 4 ROIs (grey) for each frequency of stimulation. Lines below indicate stimulus. (C) Mean number of signals per minute per ROI from the total population (endfeet, somata, and processes) following hindpaw (400 μA; 1ms; 4 Hz; for 5 s) or whisker stimulation (10 Hz, 20 Hz, 40 Hz, 90 Hz; 1 s). (D) Mean number of signals per minute per ROI from responding ROIs with and without hindpaw ($P< 0.0001$; 237 ROIs; 5 mice) or whisker stimulation (all comparisons to no stim: $P< 0.0001$; 218 ROIs; 5 mice). (E) Mean amplitude for responding ROIs comparing hindpaw ($P< 0.0001$; 237 ROIs; 5 mice) or whisker stimulation (10 Hz: $P= 0.0065$; 20 Hz: $P= 0.0418$; 40 Hz: $P< 0.0001$; 90 Hz: $P< 0.0001$; 218 ROIs; 5 mice) to no stimulation trials. (F) Mean signal duration for responding ROIs with and without hindpaw ($P< 0.0001$) or whisker stimulation (all comparisons to no stim: $P< 0.0001$). (G) Mean response probability (i.e. the fraction of trials with a peak in the activity window) following hindpaw or whisker stimulation from responding ROIs ($P< 0.0001$ for all comparisons to no stim). Bar graphs are uncorrected mean ± SEM. * $P< 0.05$, ** $P< 0.01$, *** $P< 0.001$. Statistics calculated using linear mixed models. See also Supplementary Movie 1 & 2 and Supplementary Fig. 3.

Astrocyte sub-cellular compartments respond differentially to stimulation

We also investigated the stimulus-evoked response in different astrocyte sub-cellular compartments. In the entire ROI population, whisker (90 Hz for 8 seconds) stimulation-evoked responses in endfeet and somata were masked by spontaneous activity and only processes showed a significant increase in the number of signals per minute compared to no stimulation trials ($P= 0.003$; Fig. 4A). To better study stimulus-evoked responses, responding ROIs with a peak in the activity window were identified in the endfoot, soma and process sub-populations. We first compared the mean ROI area (μm^2) for responding and spontaneous ROIs (Fig. 4B). Endfeet and somata were selected based on cellular structure, and we did not observe differences in the area of spontaneous or responding ROIs ($P= 0.999$). However, process ROIs were selected based on activity and responding processes had a larger

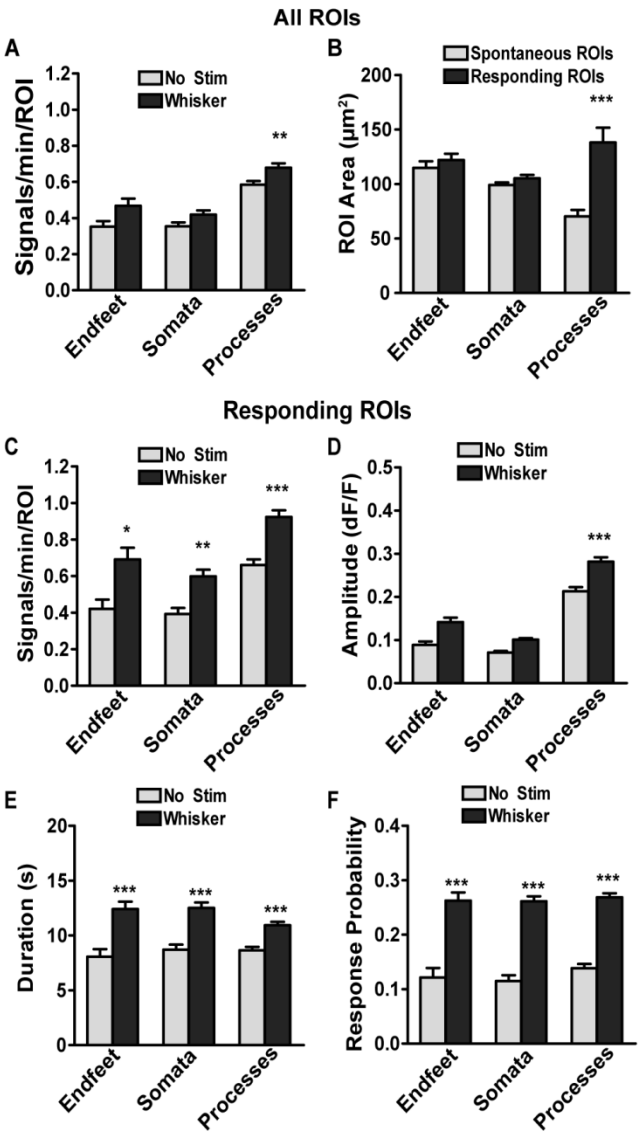

Figure 4: Astrocyte processes respond differently than endfeet and somata to sensory stimulation. (A) Mean number of signals per minute per ROI for all endfoot (n= 166 ROIs), soma (n= 403 ROIs), and process (n= 820 ROIs) ROIs following 90 Hz whisker deflection for 8 s (12 mice). (B) Mean ROI area (μm^2) for spontaneous and responding ROIs from endfeet, somata and processes. (C) Mean number of signals per minute for responding endfeet (P= 0.0224; n= 85 ROIs), somata (P= 0.0029; n= 208 ROIs), and processes (P< 0.0001; n= 420 ROIs) with or without whisker stimulation (90 Hz; 8 s). (D-F) Mean amplitude, duration and response probability for responding ROIs (endfeet, somata, and processes) with or without whisker stimulation. Bar graphs are uncorrected mean ± SEM. * P< 0.05, ** P< 0.01, *** P< 0.001. Statistics calculated using linear mixed models.

mean area than spontaneous processes (P< 0.0001; Fig. 4B), similar to light-evoked astrocyte calcium signals in the visual cortex (Asada et al. 2015). Processes also reportedly have an earlier calcium signal onset time after stimulation (Wang et al. 2006; Gee et al. 2014). When considering only the responding ROIs in each sub-cellular compartment, we found processes had the fastest mean time to reach peak maximum after 90 Hz whisker stimulation (14.41 ± 0.35 s), but there was no significant difference (P= 0.999 for all comparisons) between process, endfoot (14.73 ± 0.75 s), and soma (15.07 ± 0.51 s) peak

times. Responding processes showed an increase in mean signal amplitude upon whisker stimulation (P< 0.0001), while we did not observe a change in amplitude in responding endfeet (P= 0.2285) or somata (P= 0.3613; Fig. 4D). The number of signals per minute (Fig. 4C) and mean signal duration (Fig. 4E) increased in all responding ROI types upon 90 Hz whisker stimulation (P< 0.0001). We also observed a similar mean response probability for responding endfeet, somata and process ROIs (Fig. 4F).

Sensory stimulation induces layer-dependent changes in the relative number, not the nature, of different peak types

To investigate the underlying changes driving the overall increase in signal frequency, amplitude and duration in the different responding sub-cellular compartments, we further separated the responses by peak type and cortical layer. Upon sensory stimulation, the shape of the peak types (single peaks, multi peaks, and plateaus) did not change in amplitude or duration in any of the sub-cellular compartments (Supplementary Fig. 4). When considering the number of different peak types, the number of single peaks per minute remained unchanged in all responding ROI types (endfeet, somata or processes) and layers (Figs. 5A-C). However, somata in layer 2/3 (P= 0.0014; n= 94 ROIs; 10 mice) and processes in both cortical layers (P< 0.0001, layer 1, n= 248 ROIs; P< 0.0001, layer 2/3, n= 174 ROIs; 10 mice) had a higher number of multi peaks per minute during stimulation trials (Figs. 5E,F). Plateau signals were also prominent in responding layer 2/3 somata during whisker deflection trials (P< 0.0001; n= 94 ROIs; 10 mice; Fig. 5H). There was some evidence of an increased number of multi peaks in layer 1 endfeet (P= 0.0654; n= 41 ROIs; 10 mice; Fig. 5D) and an increased number of plateaus in layer 1 somata (P= 0.1752; n= 114 ROIs; 10 mice; Fig. 5H), but they were not significantly different from trials without stimulation.

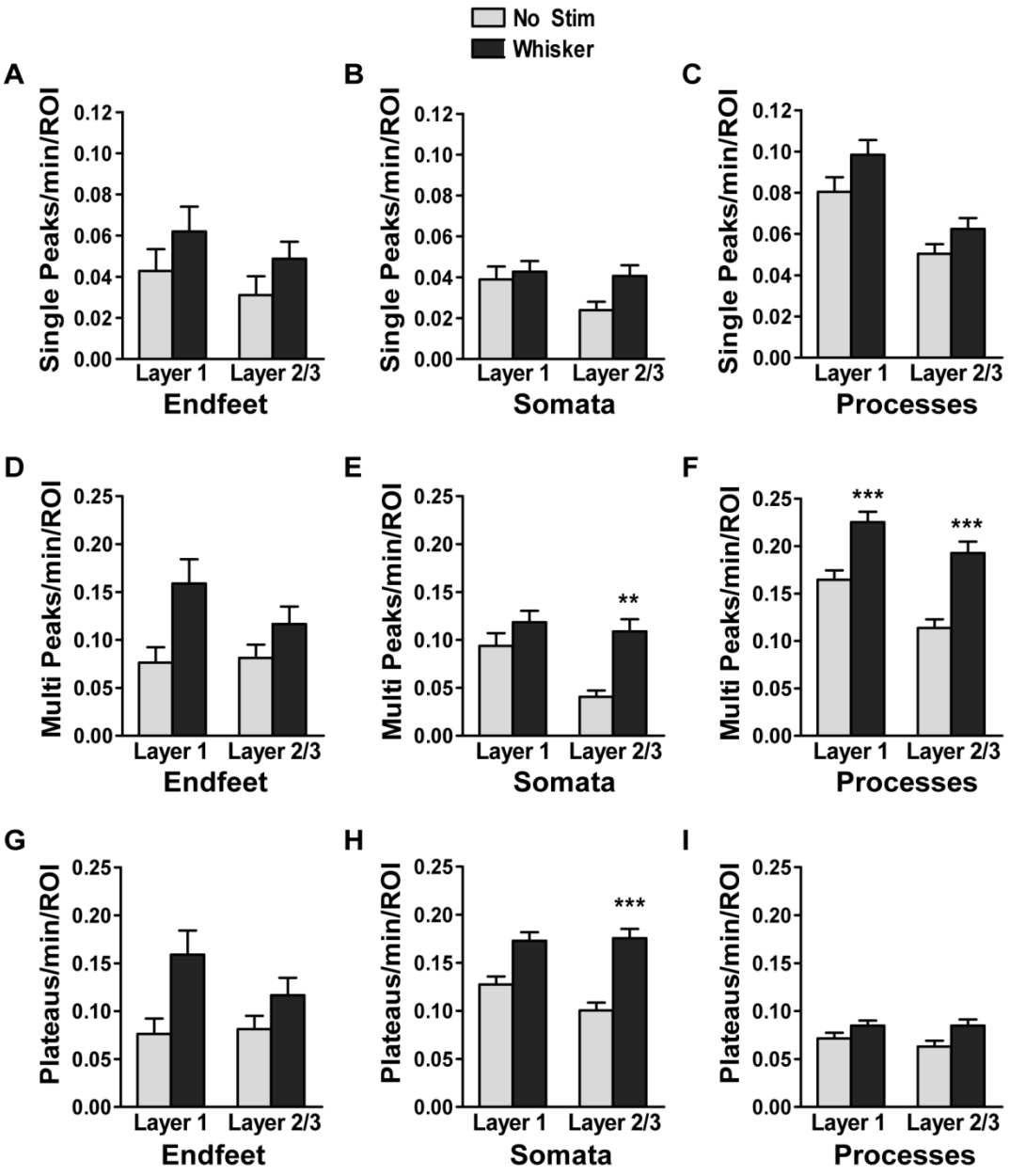

Figure 5: Responding ROIs have more signal peaks during sensory stimulation trials. (A-I) Mean number of peaks per minute, averaged across trials from each responding ROI type in layer 1 or layer 2/3 with (dark grey bars) or without (light grey bars) 90 Hz whisker stimulation (8 s). Single peaks: top row, multi peaks: middle row, plateaus: bottom row. Endfeet: left column; somata: middle column; processes: right column. Bar graphs are uncorrected mean ± SEM. ** P< 0.01, *** P< 0.001. Statistics calculated using linear mixed models. See also Supplementary Fig. 4.

Astrocytes from *Ip3r2*$^{-/-}$ mice also respond to sensory stimulation

Previous studies have shown that inositol-1,4,5-trisphosphate (IP_3)-dependent calcium release from the endoplasmic reticulum (ER) is important for astrocyte calcium signaling (Petravicz et al. 2008; Nizar et al. 2013; Takata et al. 2013; Srinivasan et al. 2015). We examined the involvement of this pathway in sensory stimulation-evoked astrocyte responses by expressing GCaMP6s in astrocytes from *Ip3r2*$^{-/-}$ mice and wild-type (WT) littermate controls (Li et al. 2005) and selecting sub-cellular ROIs in the same manner as previous experiments (manual selection for endfeet and somata ROIs and automated detection for processes). *Ip3r2*$^{-/-}$ astrocytes were less spontaneously active, as we detected fewer process ROIs in each field of view and these ROIs tended to have a smaller area (Supplementary Fig. 5A, B). We also detected fewer spontaneous single and multi peaks in *Ip3r2*$^{-/-}$ mice (Supplementary Fig. 5C). The shape of different spontaneous calcium signal peaks was not significantly different between WT and knockouts, other than a slightly decreased duration of plateau signals in *Ip3r2*$^{-/-}$cells (Supplementary Fig. 5D, E). Upon 90 Hz whisker stimulation, we were able to identify responding endfeet, somata, and process ROIs in *Ip3r2*$^{-/-}$ and WT astrocytes based on our previous criteria (peak in the activity window following stimulation; Fig. 3). *Ip3r2*$^{-/-}$ responding ROIs had an increased number of signals per minute and longer mean signal duration compared to trials without stimulation ($P< 0.0001$; Fig. 6A, C). The mean signal amplitude in responding *Ip3r2*$^{-/-}$ ROIs also tended to increase, but was not significantly different between trials with and without stimulation ($P= 0.1673$; Fig. 6B). When comparing stimulus-evoked responses from WT and *Ip3r2*$^{-/-}$ ROIs, the mean amplitude and duration were not significantly different ($P= 0.1365$ and $P= 0.5836$ respectively; Fig. 6B, C), and WT and *Ip3r2*$^{-/-}$ ROIs responded to stimulation with a similar probability ($P= 0.4456$; Fig. 6D). However, *Ip3r2*$^{-/-}$ ROIs had fewer signals per min than WT ROIs ($P= 0.0043$; Fig. 6A). When considering individual peaks, the mean time to reach peak maximum after 90 Hz whisker stimulation was similar for WT (15.77 ± 0.35 s) and *Ip3r2*$^{-/-}$ (15.79 ± 0.42 s) signals ($P= 0.1124$). Overall, peaks from each genotype that occurred during stimulation trials had a

similar peak shape (no appreciable change in amplitude or duration; data not shown). Furthermore, WT and *Ip3r2*$^{-/-}$ displayed a similar number of stimulus-evoked single peaks and plateaus in each cellular compartment and cortical layer (data not shown); however, whisker deflection evoked fewer multi peaks in *Ip3r2*$^{-/-}$ astrocyte sub-cellular compartments particularly in layer 2/3 (endfeet: WT vs *Ip3r2*$^{-/-}$, P = 0.0017; somata: WT vs *Ip3r2*$^{-/-}$, P = 0.0004; processes: WT vs *Ip3r2*$^{-/-}$, P < 0.0001; Fig. 6E-G).

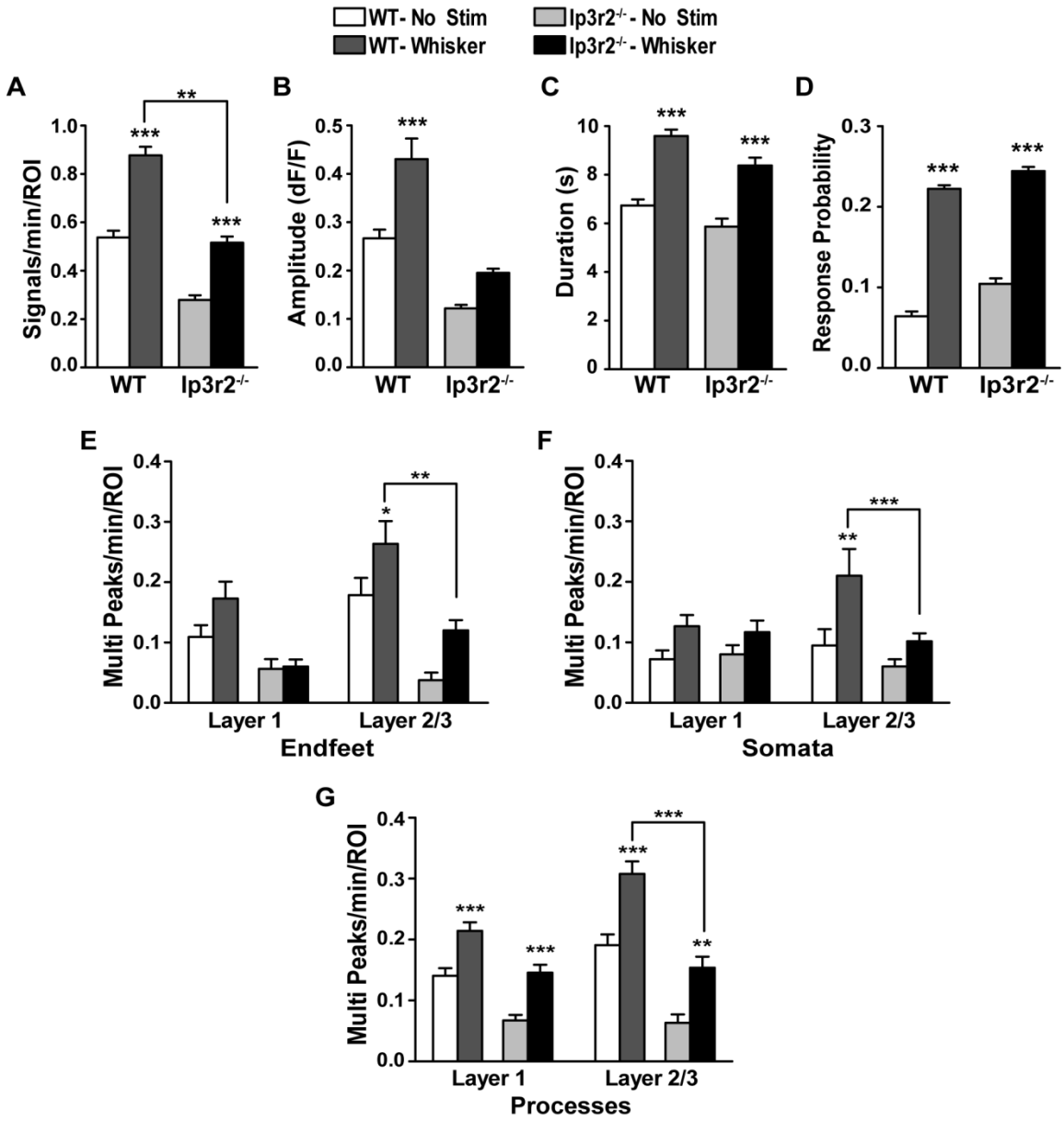

Figure 6: Astrocyte ROIs from *Ip3r2*$^{-/-}$ mice respond to sensory stimulation, but have fewer multi peak signals. (A-D) Mean number of signals per minute, amplitude, duration, and response probability for responding ROIs from wild-type (WT, n= 452 ROIs including endfeet, somata and processes; 2 mice) and knockouts (*Ip3r2*$^{-/-}$; n= 349 ROIs including endfeet, somata and processes; 3 mice) with or without whisker stimulation (90 Hz; 8 s). (E-G) Mean number of multi peaks per minute, averaged across trials from endfeet, somata, and process ROIs in layer 1 or layer 2/3 from WT and knockout mice with or without whisker stimulation (8 s). Bar graphs are uncorrected mean ± SEM. * P< 0.05, ** P< 0.01, *** P< 0.001. Statistics calculated using linear mixed models. See also Supplementary Fig. 5.

Astrocyte regions become more correlated in response to sensory stimulation

To characterize the temporal dynamics of the GCaMP6s calcium signals, we conducted a pair-wise correlation analysis on the fluorescence signal (dF/F), where traces for each ROI were compared to traces from all other ROIs in the same field of view (Fig. 7A). Overall, ROIs were weakly correlated in trials without stimulation (Pearson coefficient ρ= 0.17 ± 0.0008; n= 27956 pairs from 10 mice). The mean correlation increased upon whisker stimulation (ρ= 0.20 ± 0.0008; P< 0.0001; Fig. 7C), as shown by a shift in the cumulative fraction (Fig. 7B), suggesting an increase in network synchronicity. When we considered responding ROIs and spontaneous ROIs, we created three pair groups- spontaneous vs. spontaneous ROIs, spontaneous vs. responding ROIs and responding vs. responding ROIs. All pair groups showed an increase in correlation in trials with whisker stimulation compared to trials without stimulation (P< 0.0001); however, responding ROI pairs were significantly more correlated in stimulation trials than spontaneous pairs or spontaneous vs responding pairs (P< 0.0001, Supplementary Fig. 6A).

We also considered the pairwise signal correlations of responding ROIs separated by ROI type. Endfeet and somata pairs (endfeet vs. endfeet, somata vs. somata and endfeet vs. somata) were more correlated overall than process pairs (processes vs. processes, processes vs. somata and processes vs. endfeet; P< 0.0001; Supplementary Fig. 6B) in both no stimulation and stimulation trials. Upon whisker

stimulation, all responding ROI pairs showed an increase in correlation compared to no stimulation trials (Supplementary Fig. 6B).

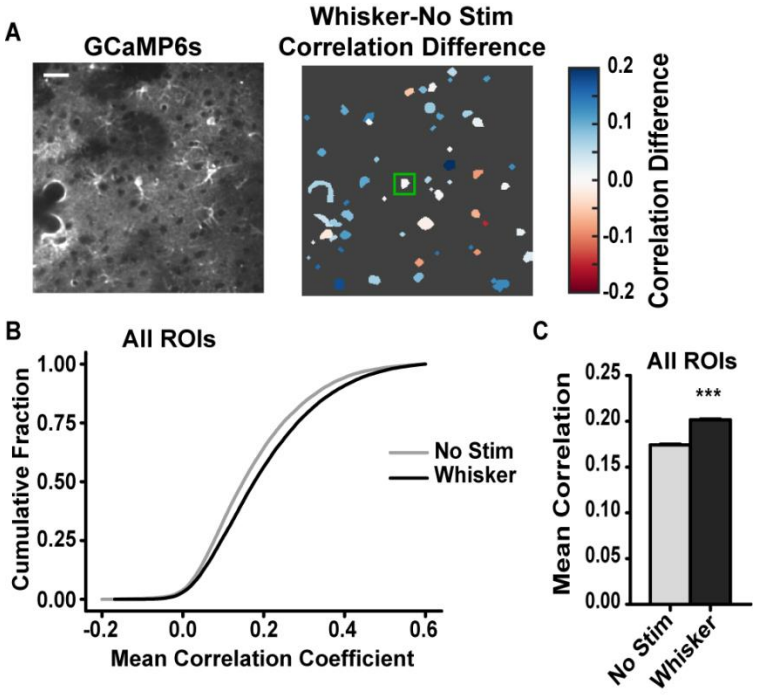

Figure 7: Astrocyte regions become more correlated upon sensory stimulation. (A) Mean pairwise Pearson correlation coefficients were calculated for all ROIs in a field of view with and without stimulation. Right: Example ROI map of the mean correlation difference (whisker stimulation coefficients - no stimulation coefficients) based on the "seed" ROI (green square). Blue colours suggest greater correlation between ROIs during stimulation and red colours suggest greater correlation between ROIs during no stimulation trials. Scale bar is 30 µm. (B) Cumulative fraction of all pairwise ROI comparisons during no stimulation or 90 Hz whisker deflection trials (n= 27307 pairs). (C) Mean correlation coefficient for all ROI pairs with and without whisker stimulation (P< 0.0001). Bar graph is uncorrected mean ± SEM. * P< 0.05, *** P< 0.001. Statistics calculated using linear mixed models. See also Supplementary Fig. 5.

Long-term stability of endfeet and somata responses

Previously, our group has shown that a neuronal sub-population consistently responds to whisker stimulation over several months (Mayrhofer et al. 2015), and we examined if astrocytes have a similar stability by imaging the same astrocyte population at different time points. Images from each session were spatially aligned to the images from the first time point (Day 0) to ensure that the field of view was the same for ROI selection across all time points (Fig. 8A). The corrected images were used to generate automated activity ROI masks for each time point, and the distances between ROI centroids

from each imaging day were compared to find ROIs with multiple occurrences (overlapping ROIs, Fig. 8B). We grouped ROIs of particular types (endfeet, somata, and processes) with multiple occurrences based on the number of days within the 4 different time points that they showed a response to stimulation (Fig. 8C). Spontaneous ROIs did not respond to stimulation on any day (0 days group). ROIs that responded to stimulation only on one day (Day 0, 4, 18 or 67) were included in the 1 day group. ROIs that demonstrated a response at two or three different time points (2 and 3 days groups) could occur on consecutive days (for example: Day 0 and Day 4) or inconsecutive days (for example: Day 0 and Day 18). ROIs within the 4 days group responded to stimulation at every time point (Day 0, 4, 18, and 67; Fig. 8C). Endfeet and somata were more stable with many ROIs responding to whisker stimulation on three (endfeet: ~31%, somata: ~16%) or four (endfeet: ~5%, somata: ~2%) imaging days. Processes were less stable with ~46% of ROIs responding only on one day and no ROIs responding on all 4 days. Responding ROIs from each time point and ROI type had a similar mean number of signals per minute across days (Fig. 8D; $P < 0.0001$ for each no stim to whisker comparison over all ROI types). Furthermore, the number of peak types (single peaks, multi peaks, and plateaus) per minute was also consistent across time points (Supplementary Figs. 7A-C).

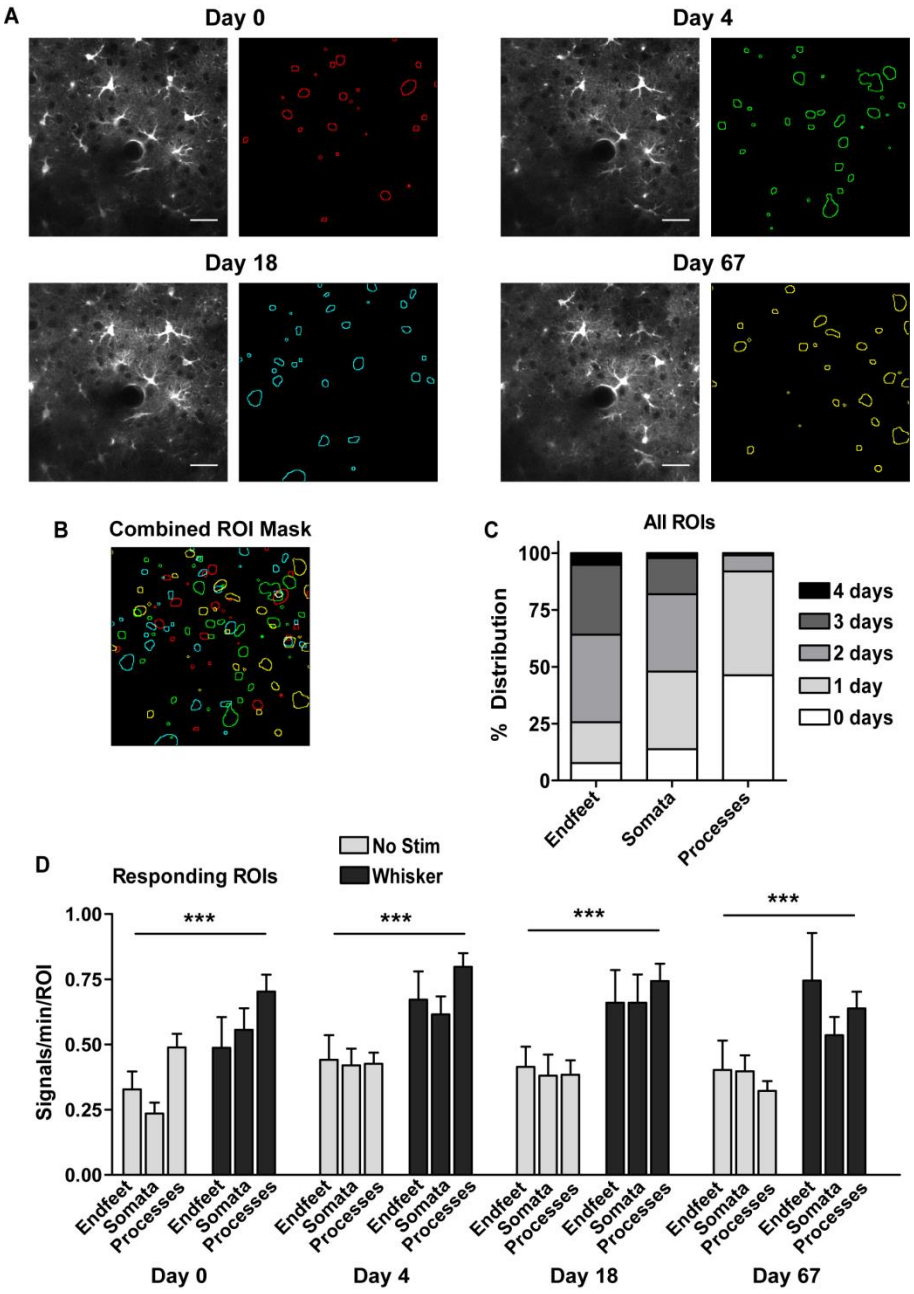

Figure 8: Astrocyte calcium responses are stable during chronic imaging. (A) Example images from the same astrocytes on different days (left) and contour outline of automated process ROI masks (right). Scale bar is 30 µm. (B) Combined ROI masks from (A) were used to identify overlapping regions. (C) The population distribution of the response frequency (number of days) for each ROI type (endfeet, somata, processes). (D) Mean number of signals per minute for responding ROIs from each ROI type ($P < 0.0001$; endfeet, somata, processes; 5 mice). Bar graphs are uncorrected mean ± SEM. *** $P < 0.001$. Statistics calculated using linear mixed models. See also Supplementary Fig. 6.

Discussion

Heterogeneous astrocyte calcium signals have been identified *in vivo* (Bonder and McCarthy 2014; Srinivasan et al. 2015); however, the nature of these signals in response to local synaptic activity remain unclear. We sought to characterize astrocyte calcium signaling in different sub-cellular compartments in terms of long-term stability and temporal synchronicity using chronic *in vivo* two-photon imaging of GCaMP6s during sensory stimulation and innovative analysis tools. These tools combined anatomical information (somata and endfeet) and activity-based region of interest selection (processes) to identify spontaneous and stimulus-evoked activity in different compartments, measured over several months. We found that a relatively large subset of astrocyte regions responded to brief, physiologically-relevant sensory stimulation (Figs. 3-4); however, these changes were driven by deviations in the relative frequency of different peak types (Fig. 5) rather than changes in the shape of individual peaks (Supplementary Fig. 4). Knockout of IP_3 receptor 2 (IP3R2), which is known to reduce calcium release from the ER, revealed a decreased number of process ROIs and multi peak signals evoked by stimulation, but did not affect the astrocytic response to stimulation as a whole (Fig. 6 and Supplementary Fig. 5). Signal synchronicity also increased upon stimulation (Fig. 7 and Supplementary Fig. 6). When we monitored long-term stability of astrocyte responses in the same field of view, the overall response was constant across several months; however, different process regions were activated on different days (Fig. 8 and Supplementary Fig. 7). These results suggest that astrocytes may stably encode local neuronal activation through distinct calcium signal peak types and coordinated activity throughout the astrocytic network, but that the location of this activity within ramified astrocyte structures may change with time.

GECIs have revolutionized astrocyte calcium imaging by providing better labelling of fine process structures compared to calcium indicator dyes that primarily label the soma (Shigetomi et al. 2013); however, the characteristics of calcium signals that have been described vary depending on the GECI

used. Early GECIs, such as Yellow Cameleon 3.60 and GCaMP3, have modest signal to noise ratios and relatively low affinity for calcium, which limited detection of spontaneous calcium microdomains within ramified astrocyte processes (Atkin et al. 2009; Paukert et al. 2014). High affinity genetic calcium indicators, such as Yellow Cameleon Nano50, detect long (~70 s) spontaneous calcium signals within astrocyte processes (Kanemaru et al. 2014), which may reflect saturation of this sensor, making it difficult to elucidate individual peaks of different types. GCaMP6s is well-suited for calcium imaging within astrocyte sub-cellular domains due to its strong signal to noise ratio and dissociation constant of 144 nM (Chen et al. 2013), which is within the astrocyte intracellular calcium concentration range (Zheng et al. 2015). With GCaMP6s, we observed localized, spontaneous calcium microdomains within process structures that have a higher mean amplitude (Fig. 1E) and a greater number of signals (Fig. 1D) than endfeet or somata, comparable to previous reports with other calcium indicators and in other brain regions (Shigetomi et al. 2013; Gee et al. 2014; Kanemaru et al. 2014; Otsu et al. 2015; Srinivasan et al. 2015; Tang et al. 2015). A previous study has also detected three different populations of GCaMP6s peaks in astrocytes: single peaks, multi peaks, and plateaus (Bonder and McCarthy 2014). We found that multi peaks were the most common peak type in fine processes, while plateaus predominated in endfeet and somata (Fig. 1K). Single peaks were found in all cellular regions (endfeet, somata and processes) and the dynamics of these peaks were similar to other reports (Bonder and McCarthy 2014).

Previously, Takata and Hirase (2008) used Oregon Green BAPTA 1-AM (OGB1) to visualize rat cortical astrocyte calcium signals *in vivo* and reported that somata in cortical layer 1 were more spontaneously active than somata in layer 2/3. We did not detect significant differences in somata, processes or endfeet spontaneous activity between layer 1 and 2/3 (Supplementary Fig. 1A-C), though layer 1 somata tended to have more signals per minute (Supplementary Fig. 1A). Takata and Hirase (2008) also reported that more astrocytes are present in layer 1 than layer 2/3 of the rat cortex, but we did not observe a difference in the number of astrocytes/mm^2 in our mice (Supplementary Fig. 1D).

These differences between rat and mouse cortical cyto-architectures could account for the discrepancies between our results.

Mice use their whiskers for vibrotactile perception mediated by high frequency changes in whisker position (Wolfe et al. 2008; Jadhav et al. 2009; Mayrhofer et al. 2015). Recently, our group characterized the neuronal population response to increasing frequencies of whisker deflection and found that while many neurons respond weakly to stimulation, a subset of highly-responding neurons (~3%) reliably discriminate different stimuli (Mayrhofer et al. 2015). In astrocytes, spontaneous signals tended to mask sensory stimulation-evoked activity within the population, particularly from whisker stimuli (Fig. 3C). We identified sub-cellular astrocyte regions that responded to sensory stimulation with a peak in the activity window, and these regions tended to be less spontaneously active and respond with more signals to different frequencies of stimulation (Fig. 3D). Based on the response probability (Fig. 3G), responding ROIs were more likely to have a peak in the activity window, but they did not respond in every trial on average, possibly due to adaptation or a local "refractory" period within the astrocyte. This refractory period may reflect local receptor inactivation in highly responsive areas, and favour activation of other regions at later times. In a previous study using different frequencies of whisker stimulation for 1 minute, local field potentials and astrocyte somata calcium responses peaked at 5 Hz and decreased at 10 Hz, which they attributed to neuronal adaptation (Wang et al. 2006). While we chose to use higher frequencies of stimulation that mimic "stick-slip" events from whisking on textured surfaces, we also limited stimulation to much shorter epochs (1 or 8 s) that reliably produce field potential spikes and calcium transients within neurons (Khatri et al. 2004; Musall et al. 2014; Mayrhofer et al. 2015). During this type of pulsatile whisker stimulation neuronal adaptation occurs within the first few pulses and the number of spikes per pulse decreases, particularly at higher frequencies (Khatri et al. 2004; Fraser et al. 2006; Musall et al. 2014). However, neuronal responses remain locked to the pulsatile stimulus (Ewert et al. 2008) and are reproducible across many trials

(Mayrhofer et al. 2015). While we did not observe a decrease in astrocyte responses with increasing whisker stimulation frequencies, neuronal adaptation could explain why the astrocytic response was not directly proportional to the stimulation intensity (10-90 Hz stimulation; Figs. 3D-F).

In terms of astrocyte compartments, a recent study compared calcium signals (from GCaMP5G) in astrocyte processes and somata during whisker stimulation and they found that somata and processes had similar mean amplitudes with a signal delay of ~25 s after the start of stimulation (Gee et al. 2014). We also found that somata, processes and endfeet had a similar mean signal onset (~15 seconds), though peaks occurred earlier after the start of stimulation. Unlike Gee *et al.* (2014), we did not observe similar somata and process signal amplitudes (Fig. 4D). We attribute this to the prevalence of low amplitude plateau signals in somata ROIs (Fig. 5H). We also observed similar response probabilities in endfeet, somata and processes (Fig. 4F), suggesting that the stimulus response was analogous across ROI types. When considering ROI area, responding process ROIs had a larger mean area than spontaneous process ROIs (Fig. 4B), similar to recent observations of light-evoked astrocyte responses in the visual cortex (Asada et al. 2015). A larger area could reflect greater propagation of signals in response to stimulation. Processes have a close proximity to synapses, and the size of astrocyte domain activation could be an integral feature of how astrocytes encode local synaptic activity. It is also worth noting that anesthetics can inhibit astrocyte calcium signals (Thrane et al. 2012), which could have suppressed the calcium responses in our experiments. However, we found that the responses were consistent across animals under isoflurane anesthesia. Future studies in awake, behaving animals that simultaneously monitor local neuronal and astrocytic calcium signals will help to better elucidate the time course and possible coordinated activity between these two cell populations.

When considering individual calcium signals, the shape of peaks (duration and amplitude) did not change upon sensory stimulation. However, we observed an increased number of multi peak and

plateau signals, which directly accounts for the differences in mean amplitude and duration that we detected between somata and processes. Somata (particularly in layer 2/3) had more plateau signals, which were of longer duration and lower amplitude, while multi peaks occurred more frequently in processes (Fig. 5), which increased the mean amplitude and number of signals per minute. Different peak types could explain how astrocytes integrate synaptic activity and may represent diverse mechanisms of signaling. Numerous pathways are known to increase intracellular calcium in astrocytes including various ion channels and calcium release from ER stores through G-protein coupled receptor-mediated IP_3 signaling or calcium induced calcium release via ryanodine receptors (Parpura et al. 2011). We specifically examined IP_3 signaling and found that, similar to a previous study (Srinivasan et al. 2015), *Ip3r2*$^{-/-}$ mice had fewer spontaneous single peaks and multi peaks. These mice also had less sensory-stimulus evoked multi peak signals (Fig. 6 and Supplementary Fig. 5). This suggests that GPCR activation and IP_3-mediated release of ER calcium stores contributes to these types of signals. However, it is important to note that even though there were fewer process ROIs detected and less multi-peak signals, the sensory-evoked astrocytic responses were not abolished in these animals and we could identify responding regions in all sub-cellular compartments without a change in response probability between knockouts and littermate controls (Fig. 6D). This indicates that other cellular mechanisms have a role in astrocyte sensory-evoked calcium signaling. Further pharmacological or transgenic mouse studies targeting different pathways of activation, will help to elucidate the contribution of these pathways to astrocyte calcium peak types.

We also observed a weak signal correlation between spontaneous astrocyte signals within the same field of view, which was similar to a previous report of correlated OGB1 activity in somata (Takata and Hirase 2008). The pairwise correlations, particularly for responding ROIs, increased upon stimulation, which suggests the population becomes more synchronous (Fig. 7). Astrocyte populations throughout the cortex are known to display widespread, coordinated calcium signaling and

synchronicity, particularly within somata, in response to norepinephrine from the locus coeruleus (Ding et al. 2013; Paukert et al. 2014) and acetylcholine from the nucleus basalis (Takata et al. 2011). In the present study, we did not observe sensory-stimulus evoked calcium signals outside the corresponding somatosensory region (Supplementary Fig. 3), suggesting these neuromodulatory pathways are not recruited by our stimulation paradigms. Increased astrocyte synchronicity after sensory stimulation could be an important component of astrocyte information processing and reflect barrel cortex circuit connectivity.

To our knowledge, we also present here the first chronic study *in vivo* of astrocyte calcium signals in the same population over time (Fig. 8). Endfeet and somata responded more stably to whisker stimulation across multiple days (Fig. 8C). Process signals tended to occur in a particular region only in a single session. It is possible that different processes are activated at different times based on the local synaptic responses (Grienberger and Konnerth 2012). Our group has previously shown that a sparse population of neurons responds reliably over different time points to whisker stimulation (Margolis et al. 2012; Mayrhofer et al. 2015). However, different synapses within the arbour of these neurons could be activated at each time point and this may cause the spatial diversity we observed in responding astrocyte processes. Signals within astrocyte processes may also induce responses in the soma and/or endfeet through second messenger cascades, allowing astrocytes to translate signals from different processes into similar calcium responses in somata or endfeet. This would account for the stable responses we observed in somata and endfeet on multiple days and could be an important feature of how astrocytes integrate synaptic information throughout the cell.

Our results provide new insights into the nature of astrocyte calcium signaling in response to sensory stimulation, particularly in terms of sub-cellular astrocyte compartmentation and different peak types. A clearer picture of calcium signaling within somatosensory astrocytes is starting to emerge: somata and endfeet respond stably to sensory stimulation over time with more plateau signals and

increased synchronicity. Processes have the greatest response to sensory stimulation and favour oscillating multi-peaks, but these signals are less synchronous and do not occur in the same process in different sessions. This helps to clarify astrocyte calcium signal heterogeneity, but raises fundamental questions about how astrocytes encode local neuronal network activity through different calcium signal peaks within different cellular compartments. Further studies correlating astrocyte and neuronal activity are now needed to better understand how astrocytes integrate synaptic frequencies.

Funding

This work was supported by the Heart and Stroke Foundation of Canada (Junior Personnel Award to J.L.S.), the University of Zurich (Forschungskredite to J.L.S., A.S.S., and M.J.P.B) and EMBO (Long-term Fellowship to A.S.S).

Acknowledgements

We would like to thank Ladina Hösli, Jean-Marc Fritschy and his lab for help with immunohistochemistry and Steven Brown and his group for molecular biology support. We would also like to thank Andrea Volterra and Ju Chen for the *Ip3r2* mouse line. B.W. is a member of the Clinical Research Priority Program of the University of Zurich on Molecular Imaging. The authors declare no competing financial interests. Address of correspondence to Jillian Stobart, Institute of Pharmacology and Toxicology, University of Zurich, Winterthurerstrasse 190, 8057 Zurich, Switzerland, Email: jstobart@pharma.uzh.ch

References

Appaix F, Girod S, Boisseau S, Römer J, Vial JC, Albrieux M, Maurin M, Depaulis A, Guillemain I, van der Sanden B. 2012. Specific in vivo staining of astrocytes in the whole brain after intravenous injection of sulforhodamine dyes. PLoS One. 7:1–13.

Asada A, Ujita S, Nakayama R, Oba S, Ishii S, Matsuki N, Ikegaya Y. 2015. Subtle modulation of ongoing calcium dynamics in astrocytic microdomains by sensory inputs. Physiol Rep. 3:e12454.

Atkin SD, Patel S, Kocharyan A, Holtzclaw L a., Weerth SH, Schram V, Pickel J, Russell JT. 2009. Transgenic mice expressing a cameleon fluorescent Ca2+ indicator in astrocytes and Schwann cells allow study of glial cell Ca2+ signals in situ and in vivo. J Neurosci Methods. 181:212–226.

Bates D, Mächler M, Bolker B, Walker S. 2015. Fitting linear mixed-effects models using lme4. J Stat Softw. 67.

Bonder DE, McCarthy KD. 2014. Astrocytic Gq-GPCR-linked IP3R-dependent Ca2+ signaling does not mediate neurovascular coupling in mouse visual cortex in vivo. J Neurosci. 34:13139–13150.

Chen T-W, Wardill TJ, Sun Y, Pulver SR, Renninger SL, Baohan A, Schreiter ER, Kerr RA, Orger MB, Jayaraman V, Looger LL, Svoboda K, Kim DS. 2013. Ultrasensitive fluorescent proteins for imaging neuronal activity. Nature. 499:295–300.

Di Castro MA, Chuquet J, Liaudet N, Bhaukaurally K, Santello M, Bouvier D, Tiret P, Volterra A. 2011. Local Ca2+ detection and modulation of synaptic release by astrocytes. Nat Neurosci. 14:1276–1284.

Ding F, O'Donnell J, Thrane AS, Zeppenfeld D, Kang H, Xie L, Wang F, Nedergaard M. 2013. α1-Adrenergic receptors mediate coordinated Ca2+ signaling of cortical astrocytes in awake, behaving mice. Cell Calcium. 54:387–394.

Ellefsen KL, Settle B, Parker I, Smith IF. 2014. An algorithm for automated detection, localization and measurement of local calcium signals from camera-based imaging. Cell Calcium. 56:147–156.

Ewert TAS, Vahle-Hinz C, Engel AK. 2008. High-frequency whisker vibration is encoded by phase-locked responses of neurons in the rat's barrel cortex. J Neurosci. 28:5359–5368.

Fraser G, Hartings J a, Simons DJ. 2006. Adaptation of trigeminal ganglion cells to periodic whisker deflections. Somatosens Mot Res. 23:111–118.

Gee JM, Smith NA, Fernandez FR, Economo MN, Brunert D, Rothermel M, Morris SC, Talbot A, Palumbos S, Ichida JM, Shepherd JD, West PJ, Wachowiak M, Capecchi MR, Wilcox KS, White JA, Tvrdik P. 2014. Imaging activity in neurons and glia with a Polr2a-based and Cre-dependent GCaMP5G-IRES-tdTomato reporter mouse. Neuron. 83:1058–1072.

Grienberger C, Konnerth A. 2012. Imaging calcium in neurons. Neuron. 73:862–885.

Hothorn T, Bretz F, Westfall P. 2008. Simultaneous inference in general parametric models. Biometrical J. 50:346–363.

Jadhav SP, Wolfe J, Feldman DE. 2009. Sparse temporal coding of elementary tactile features during active whisker sensation. Nat Neurosci. 12:792–800.

Kanemaru K, Sekiya H, Xu M, Satoh K, Kitajima N, Yoshida K, Okubo Y, Sasaki T, Moritoh S, Hasuwa H,

Mimura M, Horikawa K, Matsui K, Nagai T, Iino M, Tanaka KF. 2014. In vivo visualization of subtle, transient, and local activity of astrocytes using an ultrasensitive Ca2+ indicator. Cell Rep. 8:311–318.

Khatri V, Hartings JA, Simons DJ. 2004. Adaptation in thalamic barreloid and cortical barrel neurons to periodic whisker deflections varying in frequency and velocity. J Neurophysiol. 92:3244–3254.

Lee Y, Messing A, Su M, Brenner M. 2008. GFAP promoter elements required for region-specific and astrocyte-specific expression. Glia. 56:481–493.

Li X, Zima A V., Sheikh F, Blatter L a., Chen J. 2005. Endothelin-1-induced arrhythmogenic Ca2+ signaling is abolished in atrial myocytes of inositol-1,4,5-trisphosphate(IP3)-receptor type 2-deficient mice. Circ Res. 96:1274–1281.

Mächler P, Wyss MT, Elsayed M, Stobart J, Gutierrez R, Von Faber-Castell A, Kaelin V, Zuend M, San Martín A, Romero-Gómez I, Baeza-Lehnert F, Lengacher S, Schneider BL, Aebischer P, Magistretti PJ, Barros LF, Weber B. 2016. In Vivo Evidence for a Lactate Gradient from Astrocytes to Neurons. Cell Metab. 23:94–102.

Margolis DJ, Lütcke H, Schulz K, Haiss F, Weber B, Kügler S, Hasan MT, Helmchen F. 2012. Reorganization of cortical population activity imaged throughout long-term sensory deprivation. Nat Neurosci. 15:1539–1546.

Mayrhofer JM, Haiss F, Helmchen F, Weber B. 2015. Sparse, reliable, and long-term stable representation of periodic whisker deflections in the mouse barrel cortex. Neuroimage. 115:52–63.

Musall S, Behrens W Von Der, Mayrhofer JM, Weber B, Helmchen F, Haiss F. 2014. Tactile frequency discrimination is enhanced by circumventing neocortical adaptation. Nat Neurosci. 17:1567–1573.

Navarrete M, Perea G, de Sevilla DF, Gómez-Gonzalo M, Núñez A, Martín ED, Araque A. 2012. Astrocytes mediate in vivo cholinergic-induced synaptic plasticity. PLoS Biol. 10:e1001259.

Nizar K, Uhlirova H, Tian P, Saisan P a., Cheng Q, Reznichenko L, Weldy KL, Steed TC, Sridhar VB, MacDonald CL, Cui J, Gratiy SL, Sakadzic S, Boas D a., Beka TI, Einevoll GT, Chen J, Masliah E, Dale a. M, Silva G a., Devor A. 2013. In vivo stimulus-induced vasodilation occurs without IP3 receptor activation and may precede astrocytic calcium increase. J Neurosci. 33:8411–8422.

Otsu Y, Couchman K, Lyons DG, Collot M, Agarwal A, Mallet J-M, Pfrieger FW, Bergles DE, Charpak S. 2015. Calcium dynamics in astrocyte processes during neurovascular coupling. Nat Neurosci. 18:210–218.

Parpura V, Grubisic V, Verkhratsky A. 2011. Ca2+ sources for the exocytotic release of glutamate from astrocytes. Biochim Biophys Acta. 1813:984–991.

Paukert M, Agarwal A, Cha J, Doze VA, Kang JU, Bergles DE. 2014. Norepinephrine controls astroglial responsiveness to local circuit activity. Neuron. 82:1263–1270.

Petersen CCH. 2007. The functional organization of the barrel cortex. Neuron. 56:339–355.

Petravicz J, Fiacco T a, McCarthy KD. 2008. Loss of IP3 receptor-dependent Ca2+ increases in hippocampal astrocytes does not affect baseline CA1 pyramidal neuron synaptic activity. J Neurosci. 28:4967–4973.

Schneider CA, Rasband WS, Eliceiri KW. 2012. NIH Image to ImageJ: 25 years of image analysis. Nat Methods. 9:671–675.

Shigetomi E, Bushong EA, Haustein MD, Tong X, Jackson-Weaver O, Kracun S, Xu J, Sofroniew M V, Ellisman MH, Khakh BS. 2013. Imaging calcium microdomains within entire astrocyte territories and endfeet with GCaMPs expressed using adeno-associated viruses. J Gen Physiol. 141:633–647.

Srinivasan R, Huang BS, Venugopal S, Johnston AD, Chai H, Zeng H, Golshani P, Khakh BS. 2015. Ca2+ signaling in astrocytes from Ip3r2-/- mice in brain slices and during startle responses in vivo. Nat Neurosci. 18:708–717.

Takata N, Hirase H. 2008. Cortical layer 1 and layer 2/3 astrocytes exhibit distinct calcium dynamics in vivo. PLoS One. 3:e2525.

Takata N, Mishima T, Hisatsune C, Nagai T, Ebisui E, Mikoshiba K, Hirase H. 2011. Astrocyte calcium signaling transforms cholinergic modulation to cortical plasticity in vivo. J Neurosci. 31:18155–18165.

Takata N, Nagai T, Ozawa K, Oe Y, Mikoshiba K, Hirase H. 2013. Cerebral Blood Flow Modulation by Basal Forebrain or Whisker Stimulation Can Occur Independently of Large Cytosolic Ca2+ Signaling in Astrocytes. PLoS One. 8:4–9.

Tang W, Szokol K, Jensen V, Enger R, Trivedi CA, Hvalby O, Helm PJ, Looger LL, Sprengel R, Nagelhus EA. 2015. Stimulation-evoked Ca2+ signals in astrocytic processes at hippocampal CA3-CA1 synapses of adult mice are modulated by glutamate and ATP. J Neurosci. 35:3016–3021.

Thrane AS, Rangroo Thrane V, Zeppenfeld D, Lou N, Xu Q, Nagelhus EA, Nedergaard M. 2012. General anesthesia selectively disrupts astrocyte calcium signaling in the awake mouse cortex. Proc Natl Acad Sci. 109:18974–18979.

Volterra A, Liaudet N, Savtchouk I. 2014. Astrocyte Ca(2+) signalling: an unexpected complexity. Nat Rev Neurosci. 15:327–335.

Wang X, Lou N, Xu Q, Tian G-F, Peng WG, Han X, Kang J, Takano T, Nedergaard M. 2006. Astrocytic Ca2+ signaling evoked by sensory stimulation in vivo. Nat Neurosci. 9:816–823.

Wolfe J, Hill DN, Pahlavan S, Drew PJ, Kleinfeld D, Feldman DE. 2008. Texture coding in the rat whisker system: Slip-stick versus differential resonance. PLoS Biol. 6:1661–1677.

Zheng K, Bard L, Reynolds JP, King C, Jensen TP, Gourine A V, Rusakov DA. 2015. Time-resolved imaging reveals heterogeneous landscapes of nanomolar Ca2+ in neurons and astroglia. Neuron. 88:277–288.

Supplementary Information

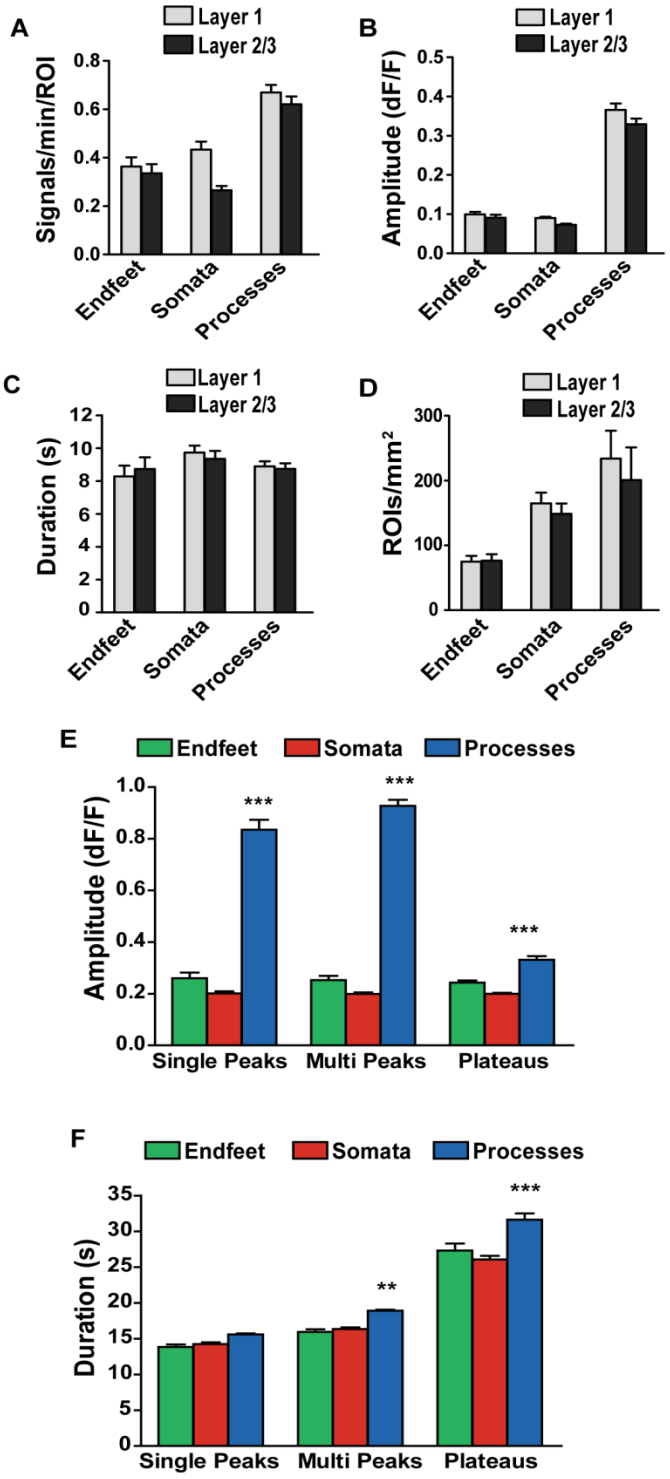

Supplementary Figure 1 (Related to Fig. 1): Astrocyte calcium spontaneity in different layers and different ROI types. (A-C) Mean signals per minute (endfeet: P= 0.9999, somata: P= 0.4449, and processes: P= 0.9969), amplitude (endfeet: P= 0.9978, somata: P= 0.8945, and processes: P= 0.8945), and duration (endfeet: P= 1.000, somata: P= 0.9977, and processes: P= 0.9737) of spontaneously active layer 1 and layer 2/3 ROIs (endfeet: layer 1, n= 91 ROIs; layer 2/3, n= 76 ROIs; somata: layer 1, n= 232 ROIs, layer 2/3, n= 161 ROIs; processes: layer 1, n= 314 ROIs; layer 2/3, n= 187 ROIs; 12 mice). (D) Mean number of endfoot, soma or process ROIs per square mm in layer 1 and 2/3 fields of view (endfeet: P= 1.000, somata: P= 0.9991, processes: P= 0.9706). (E, F) Mean amplitude (P< 0.0001) and duration (Multi peaks: P= 0.0012; Plateaus: P< 0.0001) of each peak type from different ROI types. All data are represented as mean ± SEM. ** P< 0.01, *** P< 0.001. Statistics calculated using linear mixed models.

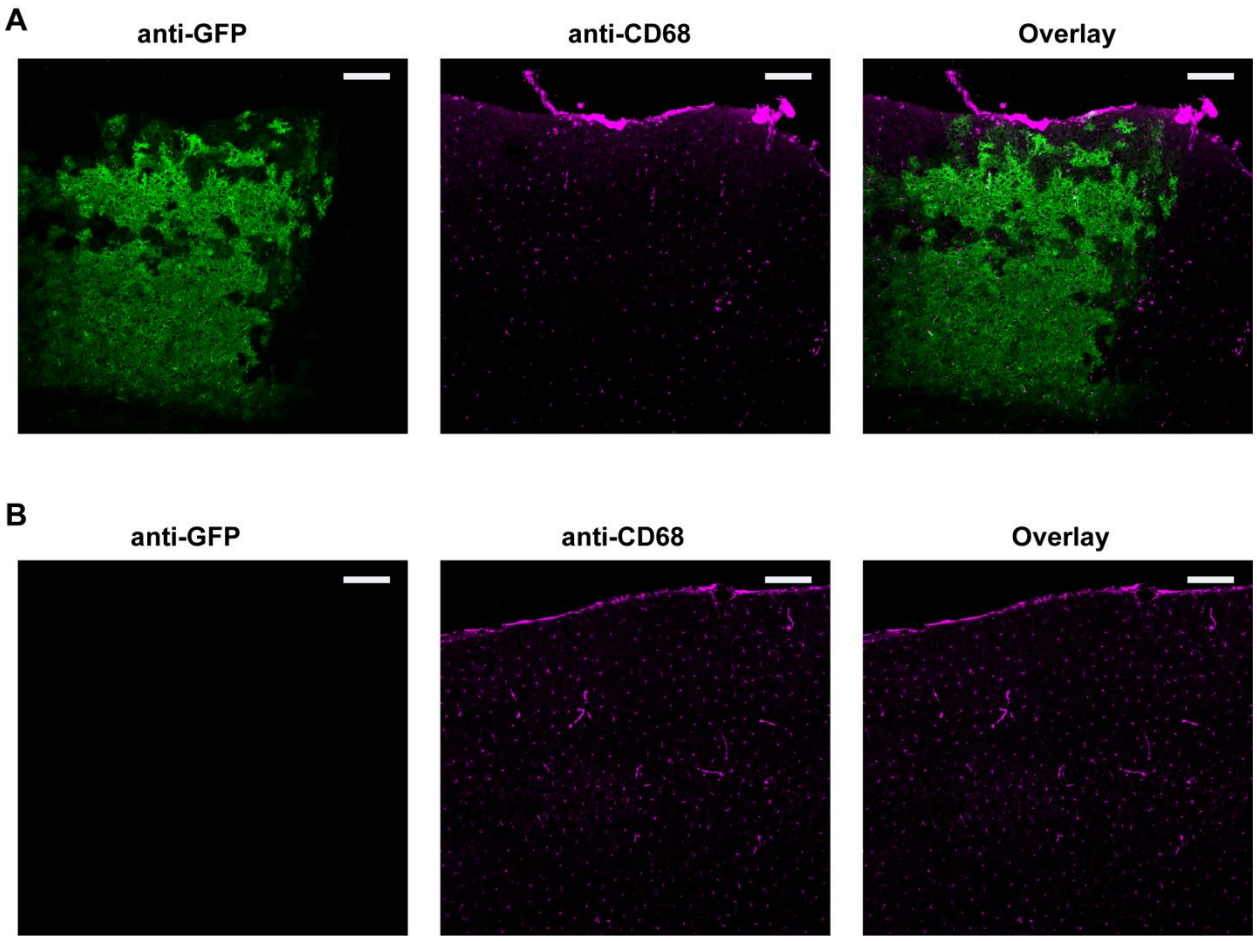

Supplementary Figure 2 (Related to Fig. 2): AAV9 virus injection and GCaMP6s expression does not activate microglia. (A) Immunohistochemistry images of brain slices from AAV9-GFAP-GCaMP6s injected mice. The virus injection site (GCaMP6s) was further stained with an anti-GFP antibody and activated microglia were labelled with CD68. (B) CD68 staining of the contra-lateral hemisphere. Scale bars are 150 µm.

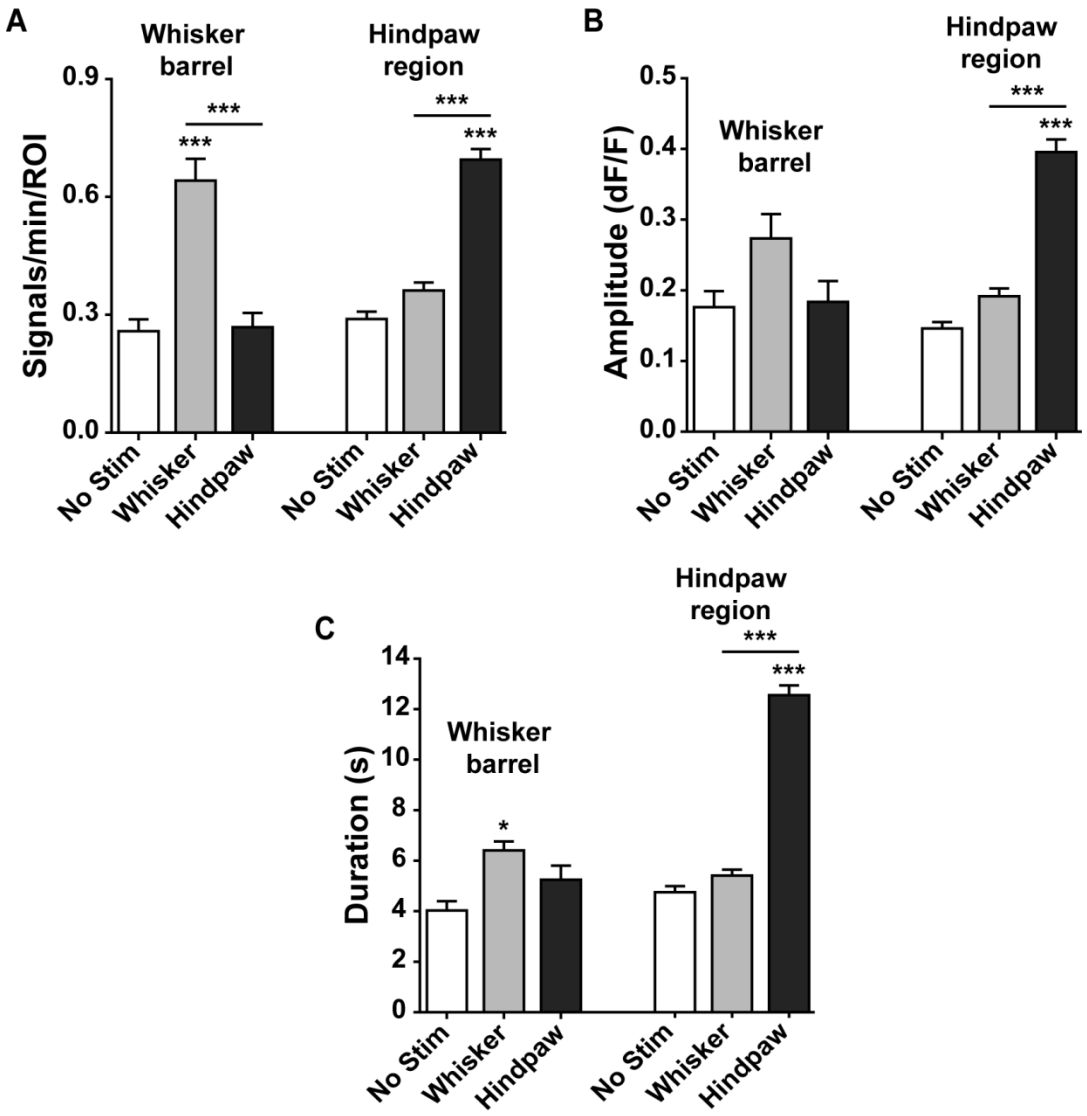

Supplementary Figure 3 (Related to Fig. 3): Astrocytes do not respond to unrelated sensory stimulation. (A) Mean number of signals per minute per ROI from responding ROIs in whisker (P< 0.0001 for 90 Hz whisker stimulation; 94 ROIs; 2 mice) or hindpaw area (P< 0.0001 for 400 µA hindpaw stimulation; 430 ROIs; 2 mice). (B) Mean amplitude comparing ROIs responding to whisker or hindpaw stimulation in whisker (P= 0.1390 for 90 Hz whisker stimulation; 94 ROIs; 2 mice) or hindpaw area (P< 0.0001 for 400 µA hindpaw stimulation; 430 ROIs; 2 mice) to no stimulation trials. (C) Mean signal duration for responding ROIs after whisker or hindpaw stimulation in hindpaw (P< 0.0001 for 400 µA hindpaw stimulation) or whisker area (P< 0.05 for 90 Hz whisker stimulation). Bar graphs are uncorrected mean ± SEM. * P< 0.05, ** P< 0.01, *** P< 0.001. Statistics calculated using linear mixed models.

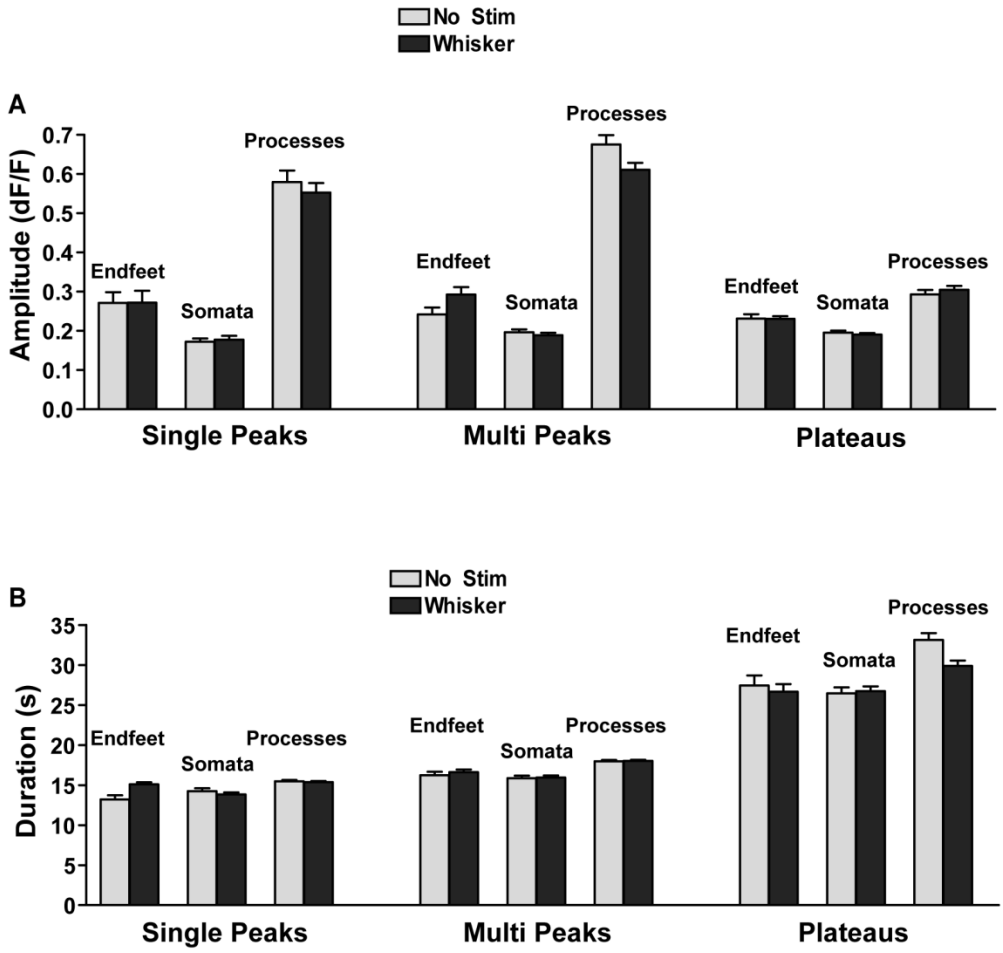

Supplementary Figure 4 (Related to Fig. 5): Calcium peak shapes do not change with sensory stimulation. (A,B) Mean amplitude and duration for single peaks (no stim: n= 705 signals; whisker: n=912 signals), multi peaks (no stim: n= 1525 signals; whisker: n= 2286 signals) and plateaus (no stim: n= 1115 signals; whisker: n= 1547 signals) for endfeet, somata, and processes averaged across trials from 10 mice. Whisker stimulation was 90 Hz for 8 sec. All data are represented as mean ± SEM. Statistics calculated using linear mixed models.

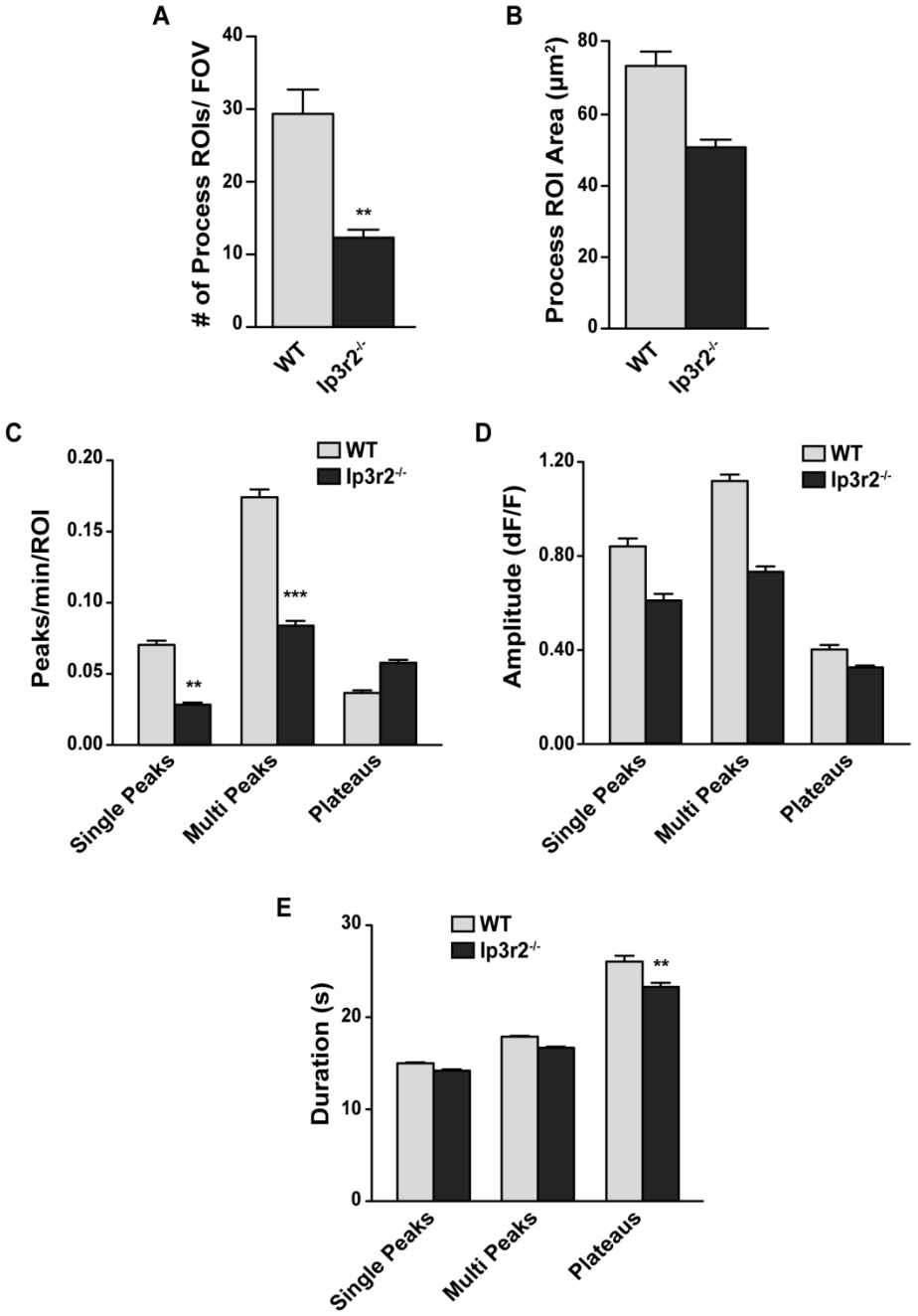

Supplementary Figure 5 (Related to Fig. 6): Ip3r2$^{-/-}$ mice display less spontaneous calcium activity. (A) Mean number of spontaneous process ROIs per field of view (FOV) detected by the automated, activity-based analysis for wild-type (WT; n= 23 FOVs; 2 mice) and and Ip3r2$^{-/-}$ mice (n= 36 FOVs; 3 mice; P= 0.0017). (B) Mean square area for process ROIs selected in the automated analysis for WT (n= 675 ROIs; 2 mice) and Ip3r2$^{-/-}$ mice (n= 443 ROIs; 3 mice; P= 0.0525). (C) Mean number of each peak type (single peaks: P= 0.0053, multi peaks: P< 0.0001, plateaus: P= 0.0719) per minute per ROI (WT: n= 1011 ROIs; 2

mice & Ip3r2$^{-/-}$: n= 986 ROIs; 3 mice). (D) Mean amplitude of the different peak types (single peaks: P= 0.96446, multi peaks: P= 0.7680, plateaus: P= 0.9978) in WT (single peaks: n= 1186 signals; multi peaks: n= 2934 signals; plateaus: n= 617 signals; 2 mice) and Ip3r2$^{-/-}$ (single peaks: n= 467 signals; multi peaks: n= 1379 signals; plateaus: n= 949 signals; 3 mice). (E) Mean duration of the different peak types (single peaks: P= 0.9623, multi peaks: P= 0.6876, plateaus: P= 0.0029) in WT (single peaks: n= 1186 signals; multi peaks: n= 2934 signals; plateaus: n= 617 signals; 2 mice) and Ip3r2$^{-/-}$ (single peaks: n= 467 signals; multi peaks: n= 1379 signals; plateaus: n= 949 signals; 3 mice). All bar graph data are represented as mean ± SEM. ** P< 0.01, *** P< 0.001. Statistics calculated using linear mixed models.

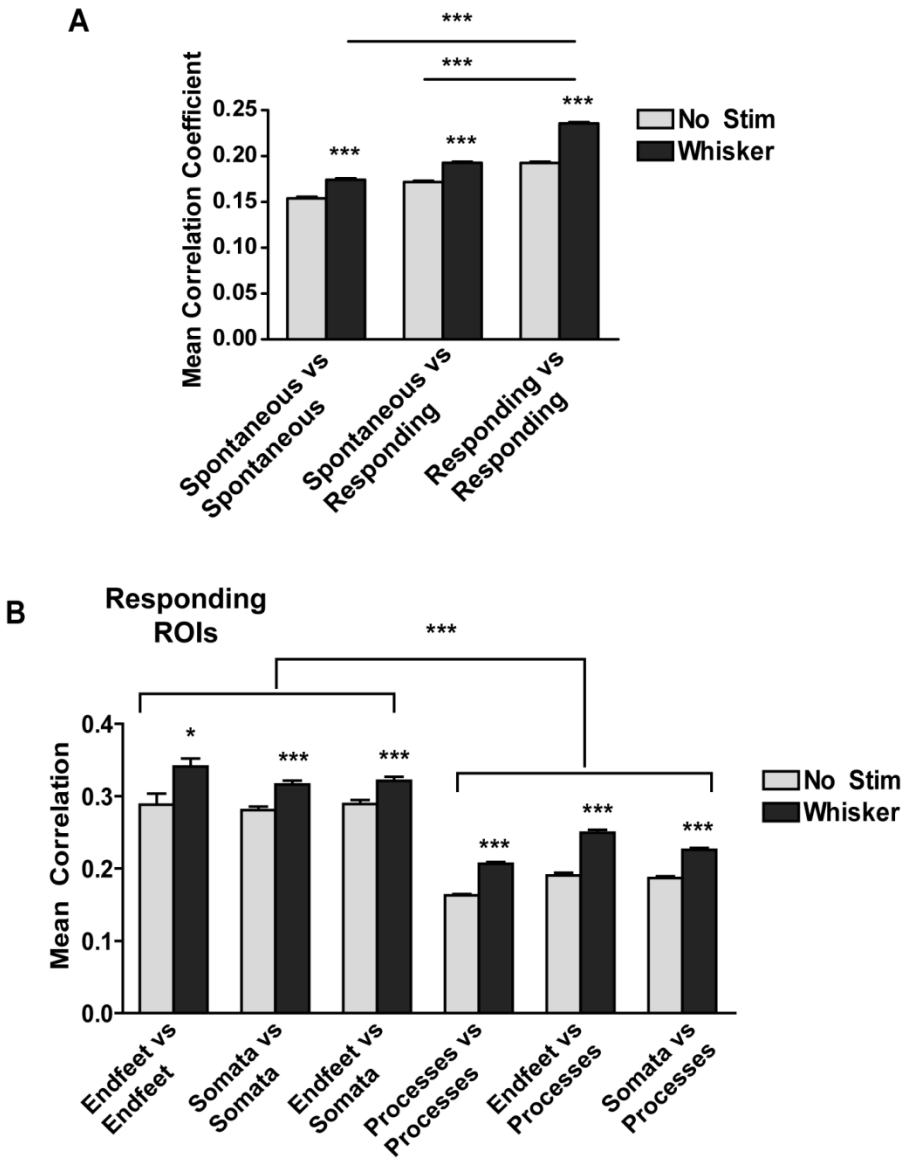

Supplementary Figure 6 (Related to Fig. 7): Responding ROIs are most correlated in stimulation trials. (A) Mean correlation coefficient for spontaneous vs spontaneous (n= 6632 pairs), spontaneous vs responding (n= 12370 pairs) and responding vs responding ROI pairs (n= 8305 pairs; 10 mice) with and without stimulation. (B) Mean correlation of pairwise responding ROIs with and without whisker stimulation of each type endfeet vs endfeet (n= 102 pairs), somata vs somata (n= 638 pairs), somata vs endfeet (n= 524 pairs), processes vs processes (n= 3407 pairs), endfeet vs processes (n= 1138 pairs) and somata vs processes (n= 2566 pairs). Statistics calculated using linear mixed models. All bar graph data are represented as mean ± SEM. * P< 0.05, *** P< 0.001. Statistics calculated using linear mixed models.

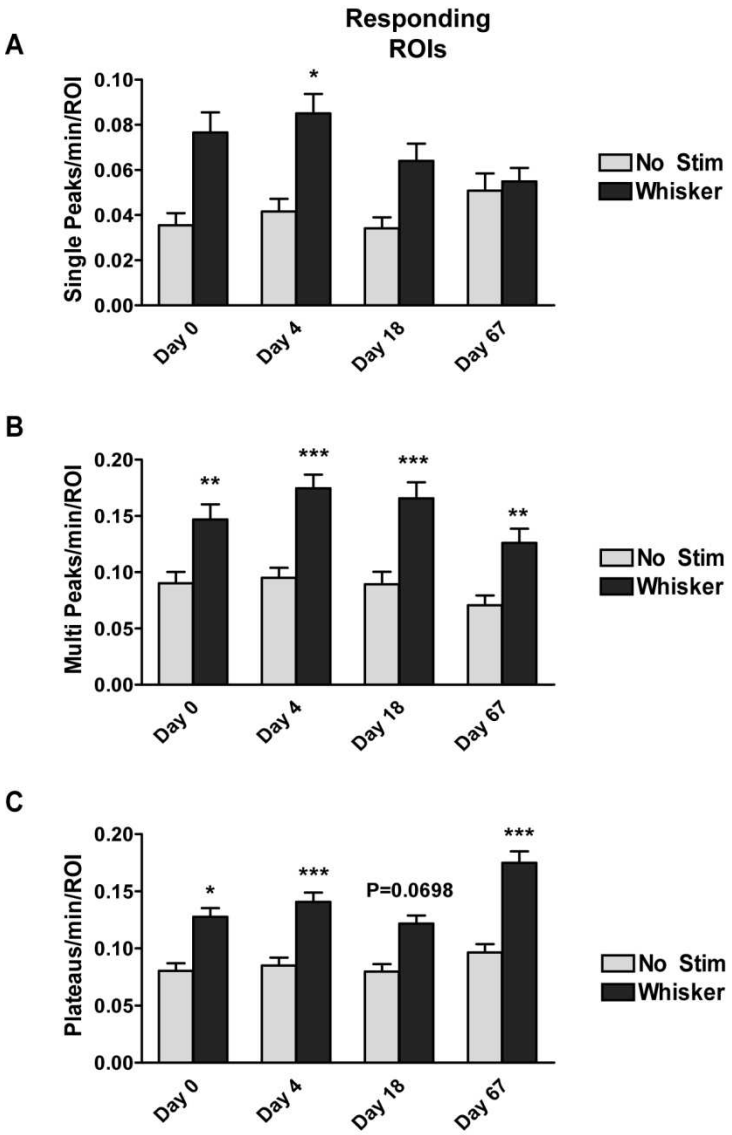

Supplementary Figure 7 (Related to Fig. 8): Number of peaks per minute do not change appreciably on different imaging days. Mean number of peaks per minute, averaged across trials from each responding ROI type with or without 90 Hz whisker stimulation (8 sec) for each time point (Day 0: n= 127 ROIs; Day 4: n= 156 ROIs; Day 18: n= 137 ROIs; Day 67: n= 130 ROIs; 5 mice). (A) The number of single peaks did not increase on Day 0, 18, and 67 upon stimulation (Day 0: P= 1296, Day 18: P= 0.6716, Day 67: P= 1.000); however, they were significantly elevated on Day 4 (P= 0.0200). (B) The number of multi peaks per ROI was also elevated after whisker stimulation for each time point (Day 0: P= 0.0011, Day 4: P< 0.0001, Day 18: P< 0.0001, Day 67: P= 0.0014). (C) The number of plateaus per ROI also increased during stimulation trials for each time point (Day 0: P= 0.0263, Day 4: P= 0.0002, Day 67: P< 0.0001) though Day 18 was not significant (P= 0.0698). Data are represented as mean ± SEM. *P< 0.05, ** P< 0.01, *** P< 0.001. Statistics calculated using linear mixed models.